Michael Stöhr, Stephan Ruoff, Bastian Rauch, Wolfgang Meier and Patrick Le Clercq, Experimental study of droplet vaporization for conventional and renewable transportation fuels: Effects of physical properties and chemical composition, Fuel 356 (2024) 129535.

The original publication is available at www.elsevier.com

https://doi.org/10.1016/j.fuel.2023.129535

© 2023. This manuscript version is made available under the CC-BY-NC-ND 4.0 license http://creativecommons.org/licenses/by-nc-nd/4.0/

Experimental study of droplet vaporization for conventional and renewable transportation fuels: Effects of physical properties and chemical composition

Michael Stöhr[a], Stephan Ruoff[a], Bastian Rauch[a], Wolfgang Meier[a], Patrick Le Clercq[a]

[a]*Institute of Combustion Technology, German Aerospace Center (DLR), Pfaffenwaldring 38-40, 70569, Stuttgart, Germany*

Abstract

As part of the global energy transition, an increasing number of sustainable liquid fuels with a wide range of physical and chemical properties becomes available for gas turbine and IC engines. For an optimal design and operation of these engines, an improved understanding of the effects of fuel properties on atomization, vaporization and combustion kinetics is required. The present work provides a comprehensive experimental study of fuel effects on droplet vaporization for numerous conventional and alternative fuels. The study employs a recently developed flow channel, where free-falling droplets with initial diameters of $D \approx 77$ μm vaporize under technically relevant gas temperatures T_g of up to 1300 K. The evolution of droplet diameters over travel distance and time is measured using microscopic shadow imaging. A total of 13 single fuel components, five bi- and tri-component mixtures, six conventional and alternative jet fuels and mixtures thereof, and three IC engine fuels and mixtures thereof have been tested under well-reproducible ambient conditions. The fuels represent a wide range of chemical classes such as n-alkanes, iso-alkanes, cycloalkanes, aromatics, alcohols and oxymethylene ethers, and most of them were measured for the first time with realistic D and T_g. The results for the single fuel components reveal in detail the temperature-dependent effects of physical properties such as boiling point T_b, liquid density ρ_l and enthalpy of vaporization H_v. In particular, it was found that for high gas temperatures of about 1250 K, the vaporization rate is almost completely determined by the product of H_v and ρ_l. By comparison with the results for single n-alkanes, the measurements for bi- and tri-component mixtures accurately characterize the preferential vaporization of individual fuel components over droplet lifetime. The results for various multi-component fuels reveal complex interplays of preferential vaporization and temperature-dependent influences of physical properties. It is shown that the vaporization for conventional and corresponding alternative fuels can differ significantly. Finally, the droplet vaporization is characterized for mixtures of PRF90+ethanol and ethanol+water, which exhibit a non-ideal vapor-liquid equilibrium.

Keywords: Liquid transportation fuels, Droplet vaporization, Effects of physical properties, Microscopic shadow imaging, Preferential vaporization

1. Introduction

The global transport sector, including road, rail, aviation, and waterborne transport, currently contributes 21% to the global CO_2 emissions, and 95% of its energy consumption is still based on fossil fuels such as oil and natural gas (figures for 2021 from Ref. [1]). Major policy makers such as the EU and USA therefore aim, among other measures, at a major increase of production and deployment of sustainable transportation fuels including electricity and various types of renewable gaseous and liquid fuels [2–4]. For modes of transport where large-scale electrification is difficult such as aviation, waterborne and heavy-duty road transport, sustainable liquid fuels are considered as a potential path to decarbonization due to their high energy density [5, 6]. For aviation, in particular, the use of seven types of sustainable aviation fuels (SAF) has been approved according to ASTM D7566 so far [5, 7], and the recent EU ReFuelEU Aviation initiative [3] and US Aviation Climate Action Plan [4] aim at a rapid scale-up of SAF production.

Renewable liquid fuels can be produced from two main feedstocks, namely biomass and electricity, and are denoted accordingly as biofuels and power-to-liquid fuels, e-fuels, or synthetic fuels, respectively. For

Email address: stephan.ruoff@dlr.de (Stephan Ruoff)

both sources, a large variety of conversion routes is available, and a broad spectrum of sustainable liquid fuels for use as renewable gasoline, diesel and kerosene can be produced [5, 6]. For road transport, bioethanol and biodiesel are already added to gasoline and diesel in many countries at different blending ratios, and renewable fuel candidates such as oxymethylene ethers (OME, also denoted as polyoxymethylene dimethyl ethers, PODE) are currently under development [8, 9]. Approved SAF include synthesized paraffinic kerosenes (SPK) made of hydroprocessed esters and fatty acids (HEFA), Fischer-Tropsch (FT)-based hydrocarbons or from alcohol (Alcohol-to-Jet, AtJ), which can be blended at up to 50% with conventional kerosene [5]. These fuel blends can then be used as so-called drop-in fuels, i.e., they can be used with existing engines and infrastructure, which is a major advantage for their utilization. Furthermore, recent field studies have shown that SAF not only reduce CO_2 emissions, but can also notably reduce non-CO_2 climate impacts such as contrail cirrus formation [10–12].

The development of renewable liquid fuels and production pathways is a highly active field of research and engineering. Due to the extensive requirements regarding storage, handling, safety, efficiency, emissions and engine performance, however, time-consuming and cost-intensive fuel testing is necessary prior to approval [13]. For the assessment of engine performance, numerous experimental and numerical works have studied the effects of alternative fuels on spray flames in various technically relevant configurations [14–30]. In general, it was found that both physical properties such as viscosity, density and boiling points as well as chemical properties such as H/C ratio and aromatic content can affect the flame stability and emissions.

Technical spray flames, however, are typically governed by a complex interplay of different subprocesses including atomization, vaporization and chemical reaction. If then, say, the NO_x emissions change when an alternative fuel is used, it is often difficult to infer whether this is due to an effect of the fuel on atomization, vaporization or chemistry. It has therefore been recognized that it is also useful to study the fuel effects on each of the subprocesses separately. Studies of effects on chemistry include, e.g., measurements of derived cetane number (DCN) [31, 32], laminar flame speeds and extinction limits [31, 33, 34], and of gas phase reactions in a shock tube [35] and variable-temperature flow reactors [34, 36, 37]. Fuel effects on atomization have been investigated using configurations relevant for IC engines [38–40], aero-engines [41, 42] and micro gas turbines [43].

Besides the effects on chemistry and atomization, fuel-dependent changes of vaporization behavior also can play an important role. Several of the aforementioned studies of fuel effects on engine performance found that the differences in the fuel vaporization can have significant effects on the stability and emission characteristics of a combustor [18–20, 23–28]. It has also been reported that preferential vaporization of individual components in multi-component fuels can have notable impacts on mixture formation and flame characteristics in technical burners and model spray flames [18, 21, 23, 44–56]. Three recent investigations have studied the dependence of the degree of preferential vaporization on various physical parameters using numerical simulations of multi-component fuel droplets. Luo et al. [55] concluded that preferential vaporization increases for lower gas temperatures T_g and at reduced ambient pressure p, whereas forced convection can cause either a decrease or increase depending on droplet Reynolds number. The work of Fredrich and Giusti [53] also found that preferential vaporization increases for lower T_g and at reduced p, and no major influence of the initial droplet diameter D_0 was observed. The study by Farouk et al. [50], on the other hand, reported a significant increase of the degree of preferential vaporization with increasing ambient pressure and initial diameter. These partly inconsistent findings highlight the complexity of the phenomenon, and motivate a desire for appropriate experimental data.

In order to include such effects of fuel composition and preferential vaporization in simulations of realistic combustors, advanced models of multi-component droplet vaporization, preferably both accurate and computationally efficient, are required [23, 47, 56]. Various types of such models, including continuous thermodynamic models (CTM) [57–60], distillation-curve models [61], discrete component models [62, 63] and quasi-discrete models [64], have been developed while this is still an active area of research, and recent works point out the need for additional measurements of multi-component droplet vaporization [23, 65].

Experimental data for vaporization of transportation fuel droplets (which often have a multi-component composition) under well-defined and technically relevant conditions, however, is still rather limited. Measurements addressing fuel composition effects were often performed at temperatures significantly below those in technical combustors or with sizes often much larger than those in real engines ($D < 100\,\mu$m), and in several cases undesired influences from suspension fibers arise [66–82]. In most of these studies, only a small number of fuels was included, and often no detailed composi-

tion of multi-component fuels was provided. The measurements of Muelas et al. [83, 84] and Honnery et al. [85], where realistic droplet diameters and gas temperatures were applied, mainly focused on droplet combustion and effects due to pyrolysis, or were restricted to few single-component fuels.

The present work addresses this need and accordingly aims at a comprehensive study of fuel effects on droplet vaporization where both droplet diameters and gas-phase temperatures are relevant for technical combustors such as gas turbine and IC engines. The study is based on experimental data from a recently designed test rig where droplets with realistic diameters of $D \approx 77$ μm vaporize in a well-defined laminar channel flow under realistic gas temperatures T_g of up to 1300 K. In a previous study, results from this test rig have been presented for six conventional or alternative jet fuels and three single-component fuels, and were compared to results from a CTM computation [86]. The present work now provides accurate data for 13 single fuel components, five bi- and tri-component mixtures, six conventional and alternative jet fuels and mixtures thereof, and three IC engine fuels and mixtures thereof. Most of them (except few reported in Refs. [83–85]) are measured for the first time with realistic D and T_g. The large number of tested fuels, all measured for the same well-reproducible conditions in the gas phase, allows for a detailed analysis of the effects of fuel physical parameters and fuel composition on the temporal dynamics of droplet vaporization. The high measuring accuracy further enables studying the effects of fuel composition on preferential droplet vaporization for numerous multi-component fuels.

At first, the experimental setup of the flow channel and measuring techniques are described in Sect. 2. Then, a brief theoretical background of droplet vaporization for single- and multi-component fuels is provided, and the relevant physical parameters are introduced in Sect. 3. Measurement results are presented and discussed in Sects. 4–6 for single fuel components, for mixtures of two or three components, and for various multi-component transportation fuels and their mixtures, respectively. Sect. 7 summarizes the main findings and conclusions.

2. Experimental setup

2.1. Laminar flow channel

The vaporization of single fuel droplets was measured in a laminar flow through a vertical channel with a cross-section of 60×60 mm^2 as shown in Fig. 1a. A stoichiometric mixture of methane and air with a mass flow of 27.3 g/min is injected into the plenum at the top and then flows downward through a water-cooled, porous bronze matrix. At the downstream surface of the matrix, a thin flat flame is stabilized, and the burned gas then flows downward through the channel. Based on exhaust gas temperature measurements for the same type of bronze matrix and for various flow rates of methane and air performed by Weigand et al. [87], an exhaust gas temperature of T_g =1891 K is obtained for the present conditions. On all four sides, the walls are made of quartz glass and are held by four posts in the corners, which provides extensive optical access.

A piezo-driven dispenser head (Microdrop MD-K-140) is installed directly above the plenum and injects single droplets into a vertical steel tube with an inner diameter of $d = 5$ mm that passes through the bronze matrix and ends 5 mm below. The end of this tube is defined as the axial position $x = 0$ mm. At the top of the vertical tube a nitrogen purge flow of 0.5 g/min and $T \approx 30$ °C is injected for rapid transport of the droplets into the hot gas below the matrix. The dispenser head is water-cooled such that its temperature remains in the range of 27–30 °C. The walls of the vertical tube inside the plenum are also water-cooled in order to prevent onset of vaporization (and thus change of fuel composition) before the droplets enter the hot gas region.

In order to ensure comparable conditions for the assessment of fuel effects, the initial droplet diameters were set to $D_0 = 77 \pm 1$ μm for all fuels. The droplets are injected periodically with a maximum frequency of 40 Hz, which results in a distance between droplets of more than 200 diameters (≈ 15 mm). For the present velocities of gas and droplets specified below, this ensures that no interaction between the droplets occurs before $x = 50$ mm where vaporization is completed. The mass flow rates of methane, air and nitrogen were measured using Coriolis flow meters with an uncertainty of 2%. The complete channel is mounted on a three-axis translation stage, in order to measure droplet diameters and velocities at different axial positions x in the channel while the measuring equipment described in Sect. 2.2 is permanently mounted.

For the assessment of the measured droplet vaporization rates, it is important to know the gas temperatures $T_g(x)$ along the droplet trajectories, i.e., the central axis of the channel ($r = 0$ mm). However, temperature measurements using optical techniques, which typically have a spatial resolution on the order of 1 mm, are difficult due to the strong radial gradients of temperature along the centerline, where temperatures can increase by up to 200 K from $r = 0$ to $r = 1$ mm

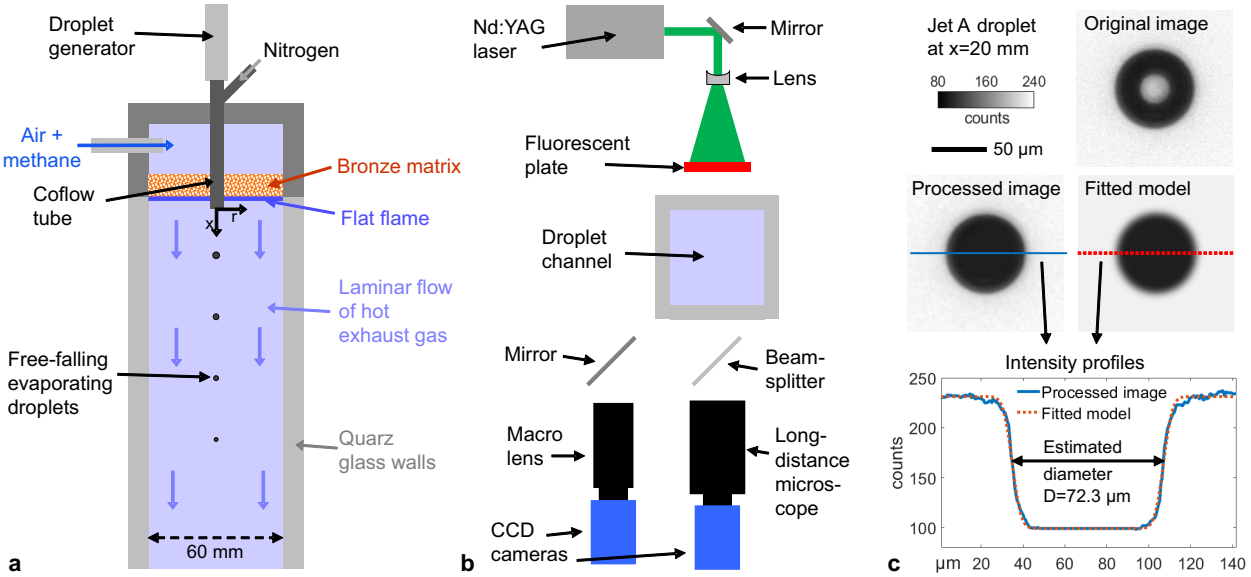

Figure 1: Schematics of a) laminar flow channel and b) shadow imaging system, and c) exemplary processing of a Jet A droplet shadow image.

[86]. Measurements using fine-wire thermocouples, on the other hand, may imply major uncertainties since radiation losses can amount to more than 100 K for T_g above 1000 K [88], and a radiation correction is difficult in the present configuration due to the simultaneous presence of a high-temperature flame close above as well as surrounding gases and side walls of unknown temperature and emissivity.

Instead of measurements, a numerical simulation of the gaseous flow in the channel has been performed in our previous work Ref. [86]. The resulting temperatures $T_g(x)$ have been used to simulate droplet vaporization for three jet fuels, and the obtained vaporization rates $K(x)$ agreed reasonably well with experiments. Additional simulations of droplet vaporization (not shown here) were performed with gas temperatures of $T_g - 50$ K and $T_g + 50$ K. The results showed that the experimental values for $K(x)$ are largely between the two numerical results for $T_g \pm 50$ K. It is therefore concluded that the simulated $T_g(x)$ are a good approximation of the real gas temperatures with deviations generally in the range of up to 50 K. The resulting gas temperatures specified in this work are rounded to multiples of 10 K. The profile of $T_g(x)$ plotted in Fig. 2 shows that T_g remains below 400 K until $x \approx 6$ mm, and then continuously increases due to radial mixing of the cold nitrogen purge flow with the surrounding hot exhaust gas of the matrix flame. At $x = 19$ mm, T_g reaches ≈ 1000 K, and then further increases to $T_g \approx 1300$ K at $x = 30$ mm and $T_g \approx 1400$ K

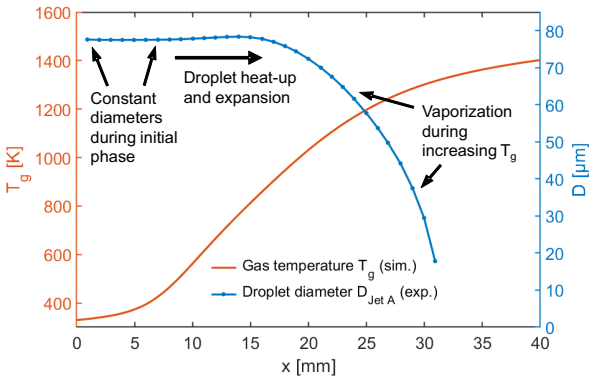

Figure 2: Gas temperature (from numerical simulation) along the centerline and evolution of measured diameter for Jet A droplets.

at $x = 40$ mm. In view of the strong radial increase of temperature mentioned above, care was taken during the experiments that radial positions of droplets are within $r \leq 0.2$ mm in order to ensure similar temperature conditions for all fuels.

Figure 2 further shows an exemplary experimental result of $D(x)$ for Jet A (the measuring techniques are introduced in Sect. 2.2). The results reveal that for $x < 8$ mm, the droplet diameters remain virtually constant. This demonstrates that during this initial phase, gas temperatures are sufficiently low such that no appreciable vaporization takes place. Therefore, it can be assumed that for multi-component fuels, the chemical composi-

tion has largely remained in the initial state and no uncertainties due to altered composition arise. This also enables numerical simulations with well-defined initial chemical composition. The measured axial velocities of the droplets along the centerline (not shown) lie in the range between 0.75 and 1 m/s for $0 < x < 50$ mm for all fuels. The axial gas velocities are, according to the simulations, typically 0–0.25 m/s lower than the droplet velocities.

2.2. Measuring techniques

The diameters and velocities of the free-falling droplets along the central axis in the gaseous flow are measured using double-pulse shadow imaging as shown in Fig. 1b. The background illumination is provided by the light pulses from a dual-cavity Nd:YAG-Laser ($\lambda = 532$ nm, $E = 2 \times 80$ mJ, $\Delta t = 50$ μs), which are widened to $d = 100$ mm using a concave lens and directed onto a fluorescent screen that emits non-coherent red light. The resulting double-images of the droplet shadow are recorded with two CCD cameras (Lavision Imager Intense) using a pellicle beamsplitter (33R/67T). On the first camera, a 200 mm macro lens is mounted, resulting in a field of view of about 9×7 mm^2 for monitoring the locations and spacing of the droplets. The second camera is equipped with a long-distance microscope (Questar QM100), resulting in a field of view of about 800×600 μm^2 for single droplet imaging. The measurement positions start at $x = 1$ mm and continue in steps of $\Delta x = 1$ mm until the droplet vaporization is completed. At each position, between 100 and 200 image pairs are recorded. An exemplary image of a Jet A droplet at $x = 20$ mm is shown in Fig. 1c, and the estimation of droplet diameters and velocities from the image pairs is described below. For the variation of x, the channel is traversed vertically while the optical setup remains fixed. The delay of the trigger signals for laser and camera relative to the timing of droplet generation is adapted for each position x such that the droplets appear in the field of view.

2.3. Data processing

A dedicated image processing routine is used to determined the diameters and velocities of the droplets from the microscopic image pairs. The process is exemplified for a Jet A droplet in Fig. 1c. As a first step, the bright spot in the center of the droplet image is removed, i.e., it is filled with the same intensity as in the region around the spot. The droplet is then represented by the model of a circle with a blurred boundary, which is obtained by convolution with a Gaussian kernel. The model parameters include the position, diameter and intensity of the circle, and the width of the Gaussian function. The optimal values of the model parameters are obtained by least-squares minimization of the differences between model and image. The resulting intensity profiles plotted at the bottom of Fig. 1c show that the droplet image is well reproduced by the model, and the method thus provides an accurate estimate of the droplet diameter and position. The change of axial positions in the image pair (not shown) further yields the axial droplet velocity $v(x)$. The conversion factor between image pixels and millimeters in the field of view is obtained from an image of a line grid with 100 μm spacing (Thorlabs R1L3S3P) taken with the long-distance microscope.

The average axial position of the droplets in the images is generally not precisely in the image center, which corresponds to the exact target position of x set by the translation stage. For each axial measurement position, the value of x is thus slightly corrected by this offset. In the discussions that follow, the values of $D(x)$ and $v(x)$ are the averages of the respective individual measurements at x. The according times $t(x)$ are calculated using the measured $v(x)$ as $t(x) = \int_{1\text{mm}}^{x} 1/v \mathrm{d}x'$. From the resulting curves of $D(t)$, the vaporization rates are determined as $K = -\mathrm{d}D^2/\mathrm{d}t$ (cf. Sect. 3.1). The temporal gradient is estimated using the standard central difference method, which gives accurate results for the generally smooth $D^2(t)$ curves.

2.4. Measurement uncertainties

The uncertainty for the measurements of droplet diameters is mainly caused by a combination of five effects: (a) errors in the optical droplet sizing (b) slight radial displacements of droplet trajectories from the centerline (which were limited to $r \leq 0.2$ mm) that can lead to higher gas temperatures for the droplets as mentioned in Sect. 2.1, (c) variations of initial droplet diameter of $D_0 = 77 \pm 1$ μm, (d) the uncertainties of mass flow meters as specified above, and (e) variations of ambient pressure of $p = 1000 \pm 30$ mbar causing changes of flow velocities of about ±3% at the given fixed mass flow rates. The latter effect could be partially compensated for by rescaling the time t with the pressure ratio 1000 mbar$/p$.

The uncertainties for the optical measurement of droplet diameters are considered to be low compared to those originating from the other effects. The resolution of the long-distance microscope is specified as 1 μm. Since for every position x 200 to 400 droplet images are taken, and the image analysis implies additional averaging along the droplet circumference, the uncertainty of

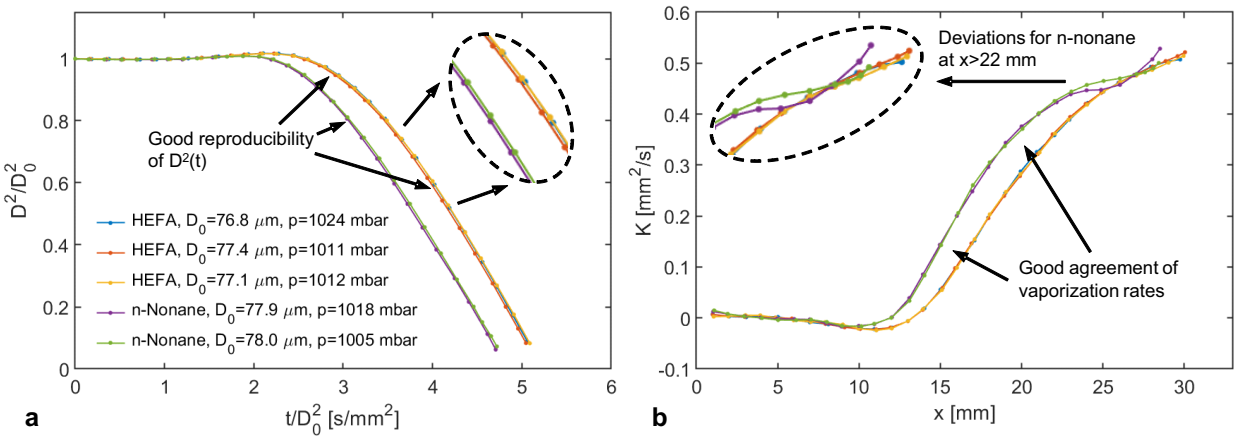

Figure 3: Comparison of repeated measurements of droplet vaporization for HEFA fuel and n-nonane.

the averaged value of $D(x)$ is estimated to be less than 0.1 μm.

The measurement errors caused by the other four effects are difficult to assess separately. Instead, the total measurement uncertainties have been estimated by repeating the measurements for some fuels. Figure 3 shows the results of three measurements for the HEFA fuel (specified in Sect. 6.1) and two measurements for n-nonane. These cases exhibit the typical variations of initial diameter D_0 and ambient pressure p. As for the discussion of the results in Sects. 4–6, the results are plotted in two ways. In Fig. 3a, the evolution of the normalized squared droplet diameter D^2/D_0^2 is plotted over the normalized time t/D_0^2, and in Fig. 3b, the vaporization rate K is plotted over the axial position x. The measured values are shown as dots connected by straight lines.

For D^2/D_0^2, the comparisons show notable, yet rather small deviations between the individual cases mainly for $t/D_0^2 > 2.5$ s/mm^2. For $K(x)$, the agreement is generally good, except for some elevated variations of K for n-nonane at $x > 22$ mm. Such variations of K for $x > 22$ mm have also been observed for some other fuels (cf. Sects. 4–6), and might be caused by small temporal drifts of droplet diameters due to slightly unstable droplet generation depending on fuel physical properties.

Overall, the comparisons in Fig. 3 demonstrate a good accuracy and reproducibility of the droplet vaporization measurements. Except for elevated variations of $K(x)$ at $x > 22$ mm for some fuels, the deviations for $D^2(t)$ and $K(x)$ between the repeated measurements are considerably lower than the respective differences between the various fuels discussed in Sects. 4–6. This is an important basis for the detailed analyses of fuel effects on droplet vaporization in Sects. 4–6.

3. Theory of droplet vaporization

3.1. Single-component fuels

As a basis for the discussion of the experimental results in the following sections, the main physical mechanisms of fuel droplet vaporization and the roles of the most relevant physical properties are briefly reviewed below. Detailed treatments of this subject can be found, e.g., in Refs. [89–92].

Generally, the droplet vaporization is governed by transport of heat and mass to and from the droplet, and the transport rates are quantified by so-called transfer numbers for heat, B_T, and for mass, B_M, respectively. For a spherical, single-component fuel droplet in a quiescent gaseous medium, these depend on the ambient gas temperature T_g, the fuel mass fraction Y_s and temperature T_s at the droplet surface, the enthalpy of vaporization H_v at $T = T_s$ and the specific heat C_{pg} of the gas according to

$$B_M = \frac{Y_s}{1 - Y_s} \quad \text{and} \quad B_T = \frac{C_{pg}(T_g - T_s)}{H_v}. \qquad (1)$$

In the following, we consider steady-state conditions after the droplet heat-up phase such that the droplet temperature is constant, and a gas phase Lewis number $\mathrm{Le} = k_g/(C_{pg}\rho_g\mathcal{D})$ of one, where k_g denotes the gas thermal conductivity, ρ_g is the gas density and $\mathcal{D}$ the diffusion coefficient of fuel vapor. In this case, the transfer numbers are equal ($B_M = B_T$) and the squared droplet diameter decreases linearly with time

as $D^2(t) = D_0^2 - Kt$, where K denotes the vaporization rate given by $K = -\mathrm{d}D^2/\mathrm{d}t$. The value of K can then be determined from B_T according to

$$K = \frac{8k_\mathrm{g}}{C_\mathrm{pg}\rho_\mathrm{l}} \ln(1 + B_\mathrm{T}) \tag{2}$$

where ρ_l denotes the liquid density.

Equation 1 shows that at a given T_g, B_T depends mainly on T_s and H_v, while the variation of C_pg with temperature is typically rather low. If, however, T_g is much higher than the fuel boiling point T_b (say, $T_\mathrm{g} - T_\mathrm{b} > 500$ K), then $T_\mathrm{s} \approx T_\mathrm{b}$ and thus $B_\mathrm{T} \approx C_\mathrm{pg}(T_\mathrm{g} - T_\mathrm{b})/H_\mathrm{v}$. It is thus expected that for $T_\mathrm{g} < T_\mathrm{b} + 500$ K, the vaporization rate K depends both on T_b and H_v, whereas for higher T_g, the influence of H_v prevails. The transition between these two regimes takes place continuously over a range of temperatures of a few 100 K. For a fuel with $T_\mathrm{b} = 200$ °C, this range lies very roughly around 1000 K, and this value will be used in the discussions in this work. The roles of physical properties in the temperature dependence of K will be further assessed using experimental results in Sect. 4.

3.2. Multi-component fuels

For fuels with two or more components, the mechanisms of droplet vaporization become more complicated. The individual components generally have different physical properties, and co-vaporize at different rates. Furthermore, the rate of vaporization and the vapor composition additionally depend on the dynamics of internal mixing in the droplet. There are two limiting regimes of internal mixing [44, 50, 93, 94]. The first is the so-called "frozen composition" regime. In this case, the rate of vaporization K is much faster than the mixing inside the droplet. The composition within the droplet then remains constant throughout the droplet lifetime, and the components co-vaporize at the surface. The other limiting case is the so-called "rapid-mixing regime", where it is assumed that internal mixing is infinitely fast or vaporization is very slow. This leads to a distillation-like vaporization, where the individual components vaporize one after another. In technical spray flames, droplet vaporization generally takes place somewhere between these two extremes [44, 50, 53]. Depending on the rate of internal mixing, a certain degree of preferential vaporization then takes place. This leads to a gradual change of liquid and vapor compositions in space and time, which in turn can have notable effects on various combustion phenomena [18, 21, 23, 44–50, 52–56]. The effects of preferential vaporization in the present experiments will be discussed in Sects. 5 and 6 using the results for fuels with two or more components.

4. Results for single-component fuels

4.1. Fuel properties

In this section, we present results for a number of single-component fuels that are typical constituents of various types of transportation fuels including those studied in the present work. The hydrocarbon components of fossil fuels such as kerosene, gasoline, Diesel and heating oil can generally be assigned to one of four main chemical classes, namely n-alkanes, iso-alkanes, cycloalkanes and aromatic species. For a number of components of each class, physical properties such as boiling point T_b, liquid density ρ_l, and enthalpy of vaporization per mass H_v and per volume $H_\mathrm{v}\rho_\mathrm{l}$ are listed in Table 1. It can be seen that the boiling points cover a wide temperature range of $98 < T_\mathrm{b} < 271$ °C that increases with the number of C atoms. The enthalpies of vaporization covering ranges of $307 < H_\mathrm{v} < 416$ kJ/kg and $211 < H_\mathrm{v}\rho_\mathrm{l} < 416$ kJ/l , on the other hand, rather depend on the chemical class. The values for $H_\mathrm{v}\rho_\mathrm{l}$, e.g., are smallest for iso-alkanes (in particular those with several branches), then increase for n-alkanes and cycloalkanes, and are highest for aromatic species.

While alcohols are generally not suitable as aviation jet fuels due to their unfavorable effects on performance and handling [95], various alcohols are commonly used as a pure or additive fuel in SI and CI engines [96, 97]. While their boiling points of $78 < T_\mathrm{b} < 158$ °C increase with the carbon number, they exhibit values of $601 < H_\mathrm{v} < 926$ kJ/kg and $493 < H_\mathrm{v}\rho_\mathrm{l} < 732$ kJ/l that are much higher than those of the hydrocarbons, and decrease with increasing carbon number. It is further noted that mixtures of hydrocarbons and alcohols may exhibit a non-ideal vapor-liquid equilibrium (VLE) that can have effects on droplet vaporization [98].

Besides alcohols, other oxygenated compounds such as oxymethylene ethers (OME_n, $\mathrm{CH_3O(CH_2O)}_n\mathrm{CH_3}$) are considered as promising additives or replacements for IC engine fuels, which have a high pollutant emission reduction potential and can be produced from sustainable sources [99, 100]. Their values of T_b for a given carbon number are higher than those of the other chemical classes, and they also exhibit the highest densities of all classes. The values of H_v are in the lower range of those for the hydrocarbons, whereas values of $H_\mathrm{v}\rho_\mathrm{l}$ are in the upper hydrocarbon range due to their high density.

While pure water is not suitable as a chemical fuel, other fuels such hydrous ethanol can contain small

Group	Species	Molecular formula	T_b [°C] at 1.013 bar	ρ_l [kg/l] at 20 °C	H_v [kJ/kg] at 20 °C	$H_v\rho_l$ [kJ/l]
n-Alkanes	n-Heptane	C_7H_{16}	98.4	0.684	368.2	251.7
	n-Octane	C_8H_{18}	125.6	0.702	367.6	258.2
	n-Nonane	C_9H_{20}	150.8	0.718	365.4	262.4
	n-Decane	$C_{10}H_{22}$	174.1	0.730	363.8	265.6
	n-Undecane	$C_{11}H_{24}$	195.9	0.740	364.5	269.7
	n-Dodecane	$C_{12}H_{26}$	216.3	0.748	364.3	272.5
	n-Tridecane	$C_{13}H_{28}$	235.4	0.757	358.2	271.2
	n-Tetradecane	$C_{14}H_{30}$	253.5	0.763	369.4	281.9
	n-Pentadecane	$C_{15}H_{32}$	270.6	0.768	372.1	285.8
iso-Alkanes[a]	2,2,4-Trimethylpentane (iso-Octane)	C_8H_{18}	99.2	0.688[b]	307.6[b]	211.6
	3-Methylnonane (iso-Decane)	$C_{10}H_{22}$	168	0.735	349.4[b]	256.9
	2,2,4,6,6-Pentamethylheptane (iso-Dodecane)	$C_{12}H_{26}$	178	0.746	287.5[b]	214.6
Cycloalkanes	Pentyl cyclopentane	$C_{10}H_{20}$	180.5	0.791	365.7	289.3
	Hexyl cyclohexane	$C_{12}H_{24}$	224.7	0.807	357.4	288.5
Aromatics	Toluene	C_7H_8	110.6	0.867	415.9	360.6
	1-Methylnaphthalene	$C_{11}H_{10}$	244.5	1.020	407.7	415.9
Alcohols	Ethanol	C_2H_6O	78.3	0.790	925.9	731.5
	1-Butanol	$C_4H_{10}O$	117.8	0.809	716.6	579.7
	1-Hexanol	$C_6H_{14}O$	157.7	0.820	601.7	493.4
OME[c]	OME_3	$C_5H_{12}O_4$	155.9	1.024[b]	359[b]	368
	OME_4	$C_6H_{14}O_5$	201.8	1.067[b]	357[b]	381
	OME_5	$C_7H_{16}O_6$	242.3	1.100[b]	349[b]	385
	OME_6	$C_8H_{18}O_7$	275	1.125[b]	347[b]	391
Others	Water	H_2O	100.0	0.998	2454	2449

[a] Values from CRC Handbook of Chemistry and Physics [103].
[b] Value for 25 °C.
[c] Values from Boyd [104]. Values for OME_6 have been estimated by extrapolation of values for OME_2-OME_5.

Table 1: Boiling point, density and enthalpy of vaporization for single-component fuels. The values are taken from VDI Heat Atlas [105] unless noted otherwise.

amounts of water [101], and the vaporization of, e.g., ethanol–water droplets can be influenced by a non-ideal VLE [65, 102]. While water has a rather low T_b of 100 °C, its value of $H_v = 2454$ kJ/kg is extremely high and can thus significantly delay vaporization. In this work, the vaporization of both pure water and ethanol–water mixtures are studied in Sects. 4.4 and 6.4, respectively.

In summary, the specifications included in Table 1 highlight the wide range of thermophysical properties of the typical components of liquid transportation fuels. The effects of these physical properties on the vaporization of single-, bi-, tri- and multi-component fuel droplets will be assessed in this and the following sections.

4.2. n-Alkanes

Figure 4 shows the measurement results for the seven n-alkanes. As is common practice in studies of droplet vaporization, the evolution of the normalized squared droplet diameter D^2/D_0^2 is plotted over the normalized time t/D_0^2 in Fig. 4a. In Fig. 4b, the corresponding rates of vaporization $K = -\mathrm{d}D^2/\mathrm{d}t$ are plotted against the travel distance x. The reason for plotting K against x is that the gas temperature T_g depends on x and not on t, and so at each position x the values of $K(x)$ refer to the same T_g for all fuels. The values of $T_g(x)$ at $x = 5, 10, ..., 30$ mm are specified at the bottom of the plot for $K(x)$.

It is seen that for $t/D_0^2 < 2$ s/mm^2, the diameters at first remain constant and then start to increase (and thus K becomes negative). This shows that during this phase, where temperatures start rising but still remain rather

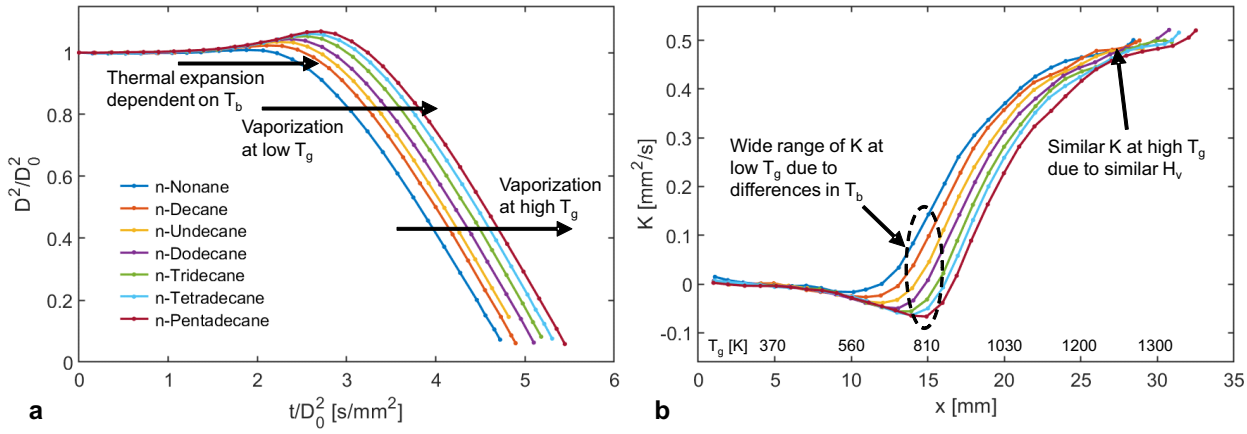

Figure 4: a) Temporal evolution of normalized squared droplet diameter and b) axial evolution of droplet vaporization rate for seven n-alkanes.

low (Fig. 2), the droplets mainly heat up towards their respective boiling point, and the diameter increases due to the reduced liquid density. The thermal expansion is highest and takes longest for n-pentadecane since it has the highest boiling point and thus it takes the longest to heat up. After the heat-up, the diameters decrease due to vaporization, and the values of $K(x)$ continuously increase due to the continuous rise in gas temperature. For $10 < x < 20$ mm, where intermediate temperatures ($560 < T_g < 1030$ K, cf. Fig. 2) prevail, the vaporization rates $K(x)$ vary significantly for the different n-alkanes. This corresponds to their wide range of boiling point T_b, which governs the vaporization at these temperatures as discussed in Sect. 3.1. For $x > 25$ mm, by contrast, the values of K are similar for all n-alkanes. This is because for the high temperatures in this region ($T_g > 1200$ K), the vaporization rate now mainly depends on the enthalpy of vaporization H_v, which is similar for all n-alkanes. Overall, the physically consistent variation of the droplet vaporization curves for the n-alkanes highlights the high accuracy of the measurements and the good reproducibility of ambient conditions.

4.3. Alcohols

Compared to the n-alkanes, the alcohols exhibit much higher values of H_v as listed in Table 1. Furthermore, it is important to note that the values of T_b and H_v for the alcohols change in opposite ways, i.e., T_b increases while H_v decreases as the carbon number increases.

Figure 5 shows the evolution of droplet vaporization for the three alcohols ethanol, 1-butanol and 1-hexanol, together with the results for n-nonane and n-pentadecane for comparison. It can be seen that in the range $8 < x < 17$ mm with relatively low gas temperatures, the vaporization rates K are governed by T_b such that ethanol vaporizes fastest followed by 1-butanol and 1-hexanol. After $x = 18$ mm, however, this trend is completely reversed and now 1-hexanol has the highest K. This is due to 1-hexanol having the lowest H_v, which is the dominant physical parameter for $T_g \gtrsim 1000$ K as discussed in Sect. 3.1 and seen for the n-alkanes before. Over the full droplet lifetime, these opposite trends largely cancel out, and (for the present test conditions) all three alcohols have almost the same lifetime as shown in Fig 5a. It can also be seen that their lifetimes are at the upper end of the n-alkane lifetimes, which is mainly due to the significantly higher values of H_v for the alcohols.

4.4. Aromatics and water

Finally, in Fig. 6 results are plotted for two aromatic compounds that are typical components of fossil fuels, namely the monocyclic toluene and the bicyclic 1-methylnaphthalene, as well as for (distilled) water. The curves for two n-alkanes and two alcohols are also included for comparison. As discussed in Sect. 4.1, the values of T_b for the two aromatic species (111 and 245 °C) are in the same range as those of n-alkanes, whereas their values of H_v and $H_v\rho_l$ are higher than those of the other classes of hydrocarbons. Water has a rather low T_b of 100 °C, while its value of $H_v = 2454$ kJ/kg is extremely high. The remarkably long lifetime of the water droplets compared to the other compounds seen in Fig. 6a demonstrates that even small concentrations of water in fuels such as hydrous ethanol can have a notable effect on droplet lifetime, as discussed further in Sect. 6.4.

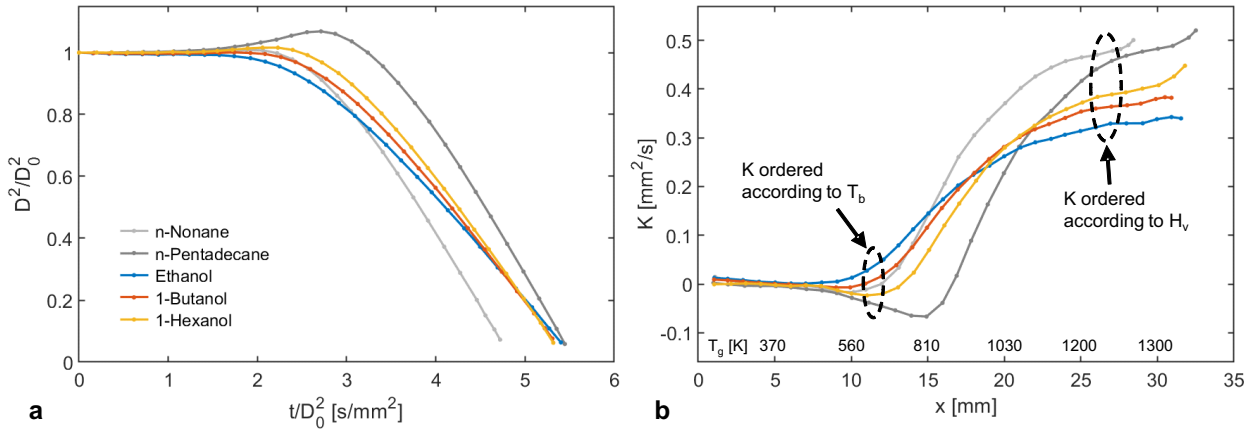

Figure 5: a) Temporal evolution of normalized squared droplet diameter and b) axial evolution of droplet vaporization rate for three alcohols and two n-alkanes.

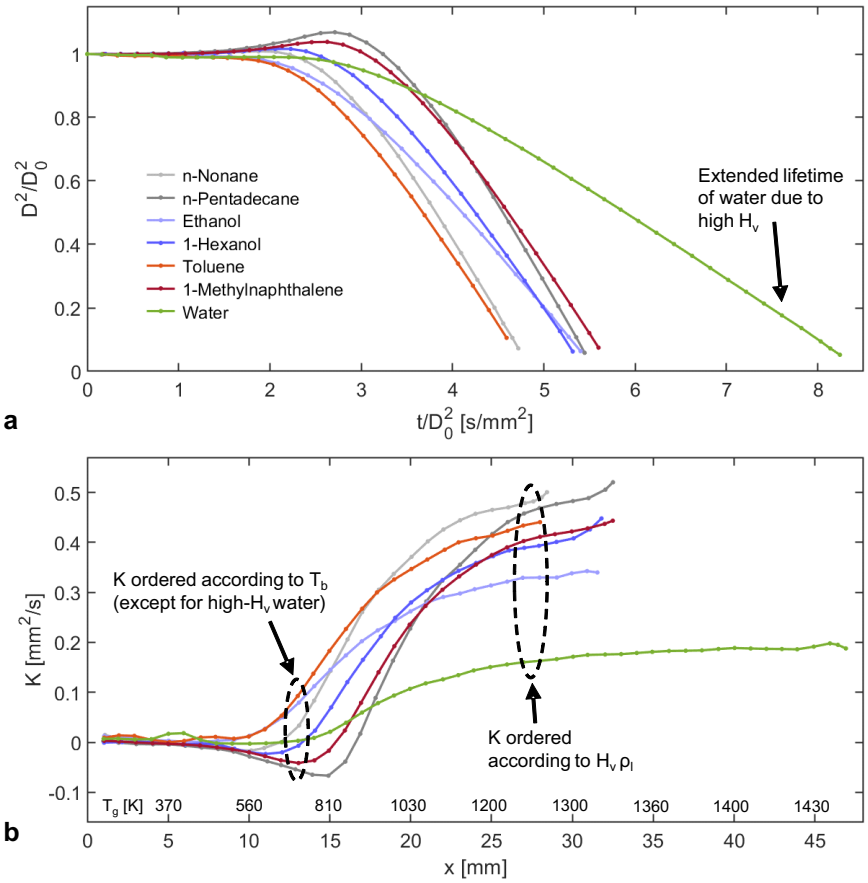

Figure 6: a) Temporal evolution of normalized squared droplet diameter and b) axial evolution of droplet vaporization rate for two aromatic compounds, water, two alcohols and two n-alkanes.

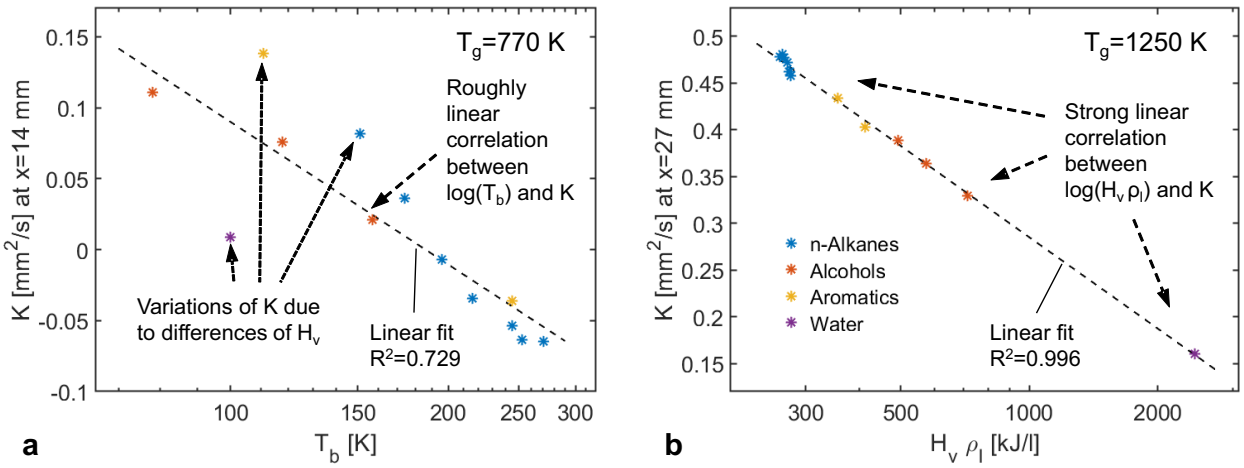

Figure 7: Correlation of vaporization rates K with a) boiling points T_b at $x = 14$ mm and with b) enthalpy of vaporization per volume $H_\mathrm{v}\rho_\mathrm{l}$ at $x = 27$ mm for single-component fuels.

The results for $K(x)$ shown in Fig. 6b largely confirm the temperature-dependent effects of T_b and H_v discussed before. For the lower gas temperatures at, say, $x = 13$ mm, the vaporization rates have the same order as the boiling points except for water, where K is reduced due to the very high H_v. For increasing x, this trend changes and the curves for $K(x)$ often intersect. At the end, for the highest gas temperatures of $T_\mathrm{g} > 1220$ K at $x > 26$ mm, the vaporization rates are then mostly ordered in the same way as the values of H_v, demonstrating again the strong effect of H_v on K at these high T_g. The values of the enthalpy of vaporization per mass H_v, however, cannot explain the higher K of toluene compared to 1-methylnaphthalene. The values of the enthalpy of vaporization per volume $H_\mathrm{v}\rho_\mathrm{l}$ (cf. Table 1), by contrast, have exactly the same (opposite) order as the values of K at $x > 26$ mm, indicating that $H_\mathrm{v}\rho_\mathrm{l}$ has a stronger effect on K than H_v at the these high gas temperatures. This finding is discussed in more detail below.

4.5. Temperature-dependent roles of T_b and H_v

The theoretical analysis in Sect. 3.1 has shown that the vaporization rate K of single-component fuel droplets generally depends on several physical fuel properties such as T_b, H_v, ρ_l and C_pg. The discussion also indicated that for gas temperatures below $\approx$ 1000 K, K is more dependent on T_b, and for $T_\mathrm{g} \gtrsim 1000$ K, the influence of H_v is stronger. These temperature-dependent effects of T_g and H_v on K have also been seen in the measurement results presented in the previous subsections.

In the following, the temperature-dependent roles of T_b and H_v will be assessed in more detail using the measurements of $K(x)$ for all 13 single-component fuels, which cover a wide range of physical properties (cf. Table 1). To this end, correlations of K with T_b, H_v and $H_\mathrm{v}\rho_\mathrm{l}$ have been evaluated at each axial position x. Both the enthalpy per mass, H_v, and per volume, $H_\mathrm{v}\rho_\mathrm{l}$, were included in order to compare their influence. Figure 7 shows two exemplary results, namely the correlation of K vs. T_b at $x = 14$ mm, where a relatively low gas temperature of $T_\mathrm{g} = 770$ K is present, and a plot of K vs. H_v at $x = 27$ mm where $T_\mathrm{g} = 1250$ K is much higher. In both cases, the x-axis is plotted logarithmically according to the logarithmic dependence of B_T on $T_\mathrm{b} \approx T_\mathrm{s}$ and H_v in Eq. (1).

The plot in Fig. 7a shows a roughly linear correlation ($R^2 = 0.729$) between K and $\log(T_\mathrm{b})$ at $x = 14$ mm ($T_\mathrm{g} = 770$ K), which confirms the theoretically expected, significant influence of T_b on K at such relatively low gas temperatures (cf. Sect. 3.1). At the same time there are still considerable deviations from the linear correlation, and it is seen that fuels with higher H_v have lower values of K. This is in line with theory and indicates that while T_b has the strongest influence on K at this temperature condition, the effects of H_v are still notable and cannot be neglected.

At $x = 27$ mm ($T_\mathrm{g} = 1250$ K), by contrast, the plot of K versus $\log(H_\mathrm{v}\rho_\mathrm{l})$ in Fig. 7b reveals an excellent linear correlation with $R^2 = 0.996$. This shows that for such elevated temperatures, the vaporization rate K of a droplet is almost completely governed by the values of $H_\mathrm{v}\rho_\mathrm{l}$ at 20 °C. A similar correlation of K versus $\log(H_\mathrm{v})$

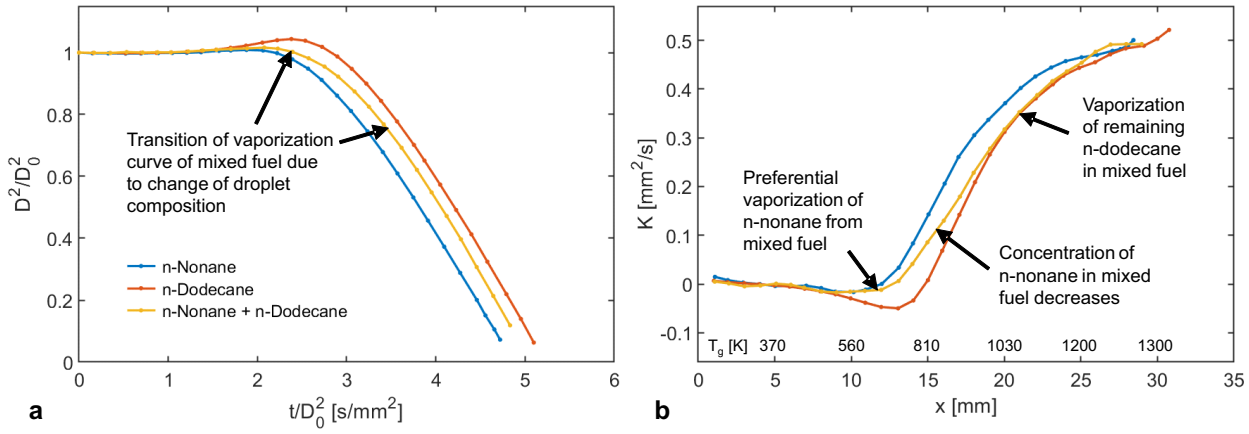

Figure 8: a) Temporal evolution of normalized squared droplet diameter and b) axial evolution of droplet vaporization rate for pure n-nonane, pure n-dodecane, and 1:1 (by vol.) mixture of both.

at $x = 27$ mm (not shown) also reveals a strong, but somewhat reduced linear correlation with $R^2 = 0.836$, indicating that K also slightly depends on ρ_l. It is also noted that for lower gas temperatures, e.g. $T_g = 1110$ K at $x = 22$ mm, the R^2 value for the correlation of K versus $\log(H_v\rho_l)$ (not shown) reduces significantly to $R^2 = 0.864$, indicating that K is then also influenced by other properties.

While the theoretical considerations in Sect. 3.1 already indicated the dominant effect of H_v on K at high temperatures, the almost exclusive dependence of K on $H_v\rho_l$ at $T_g = 1250$ K seen in Fig. 7b is a remarkable result that has, to our knowledge, not been reported before. It suggests that for gas temperatures at (and possibly also above) 1250 K, the influences of other liquid fuel properties such as T_b, and gas phase properties such as C_{pg} and k_g can largely be neglected. While this finding is for now only applicable to the present test conditions ($T_g = 1250$ K, atmospheric pressure and low droplet velocity), the result may in principle enable more efficient computations of K based on a reduced number of physical parameters, which might be beneficial for simulations of spray flames with a large number of droplets.

5. Results for bi- and tri-component fuels

5.1. Mixture of n-nonane and n-dodecane

In this section, results are presented for fuel mixtures made of two or three chemical components. These measurements are considered as an intermediate step between single- and multi-component fuels, and their purpose is to identify the regimes of internal mixing and the occurrence of preferential vaporization (cf. Sect. 3.2).

Figure 8 shows the droplet vaporization for a mixture of n-nonane and n-dodecane (each 50% by vol.) together with the results for pure n-nonane ($T_b = 151$ °C) and pure n-dodecane ($T_b = 216$ °C). The droplet diameters of the mixture always remain between those of the pure components while slightly shifting over time towards the less volatile n-dodecane. The plots of $K(x)$ in Fig. 8b show that the vaporization rate of the mixture remains equal to that of n-nonane until $x = 11$ mm, demonstrating that until this position, mostly n-nonane vaporizes. Subsequently the vaporization rate continuously approaches that of n-dodecane, indicating that the composition of the vaporizing fuel also shifts towards n-dodecane. Starting from $x = 20$ mm, the vaporization rate is equal to that of n-dodecane, which shows that in this final phase, only n-dodecane is left in the droplet. This behavior can be described neither by the frozen-composition mode nor by the distillation-like (i.e., step-like) mode of two-component vaporization. Instead, the continuous transition of $K(x)$ for the mixture suggests that the rate of internal mixing lies somewhere near the middle between these two modes.

The finding that $K(x)$ of the mixture is close to that of the more volatile n-nonane during the initial phase, and later approaches the values for the less volatile n-dodecane, clearly indicates that pronounced preferential vaporization of the more volatile n-nonane takes place during the early stages of vaporization. The results thereby demonstrate that preferential vaporization in a fuel mixture can be identified by comparing the $K(x)$ curve of the mixture with the respective curves for indi-

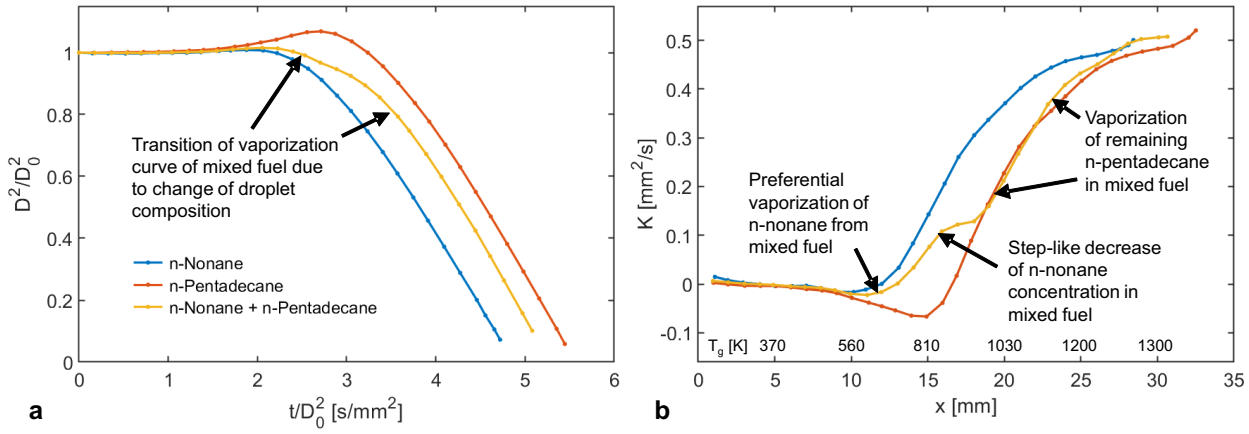

Figure 9: a) Temporal evolution of normalized squared droplet diameter and b) axial evolution of droplet vaporization rate for pure n-nonane, pure n-pentadecane, and 1:1 (by vol.) mixture of both.

vidual components. This will be used for the analyses of vaporization of fuel blends in the following sections. In view of the strong variation of $T_g(x)$ and its complex fuel-dependent effects on $K(x)$, however, no quantitative assessment of the degree of preferential vaporization (as performed e.g. by Farouk et al. [50] for burning jet fuel droplets) is attempted in this study.

5.2. Mixture of n-nonane and n-pentadecane

In Fig. 9, results are shown for a mixture of n-nonane and n-pentadecane (each 50% by vol.) and compared to the measurements for pure n-nonane (T_b = 151 °C) and n-pentadecane (T_b = 271 °C). For this combination, the difference in boiling point for the two components is much larger than for the mixture with n-dodecane discussed above. The evolution of $K(x)$ shows that similar to the case with n-dodecane, mostly n-nonane vaporizes during the early phase, and in the later phase only the heavier component, now n-pentadencane, remains in the droplet. The vaporization rate is now equal to that of n-pentadecane already at x = 18 mm. Compared to the case with n-dodecane, the transition is thus more step-like, i.e., the vaporization is now more distillation-like. These results suggest that the preferred vaporization of the more volatile component (in this case n-nonane) is further enhanced when the boiling point of the heavier component is higher. This indicates that among other parameters such as droplet size and gas temperature (cf. Sect. 3.2), the chemical composition also has a major effect on the degree of preferential vaporization.

5.3. Mixtures of three n-alkanes

Additional measurements for three different mixtures of three n-alkanes each have been performed in order to further investigate effects of fuel composition on preferential vaporization. Each mixture contains n-dodecane and two other n-alkanes, one with a higher and one with a lower boiling point, and the share is 33% by vol. each. Three mixtures, namely (n-C11+n-C12+n-C13), (n-C10+n-C12+n-C14) and (n-C9+n-C12+n-C15) were chosen that exhibit an increasing range of boiling points (cf. values of T_b in Table 1).

The measurement results for the three mixtures and for pure n-dodecane are plotted in Fig. 10. The latter results are the reference case where no preferential vaporization occurs. For the mixture (n-C11+n-C12+n-C13) with the smallest range of T_b, the results closely follow the curves for pure n-dodecane, indicating that virtually no preferential vaporization takes place. For the other two mixtures, the curves for $K(x)$ exhibit an increased vaporization of the light components at 10 < x < 16 mm and reduced vaporization of the heavy component at 16 < x < 25 mm. For x > 25 mm, values of K are similar for all mixtures since vaporization is mainly governed by H_v for the high temperatures in this region, as discussed in Sect. 3.1. Overall, the results for the three tri-component mixtures highlight the notable effect of the range of boiling points on the extent of preferential vaporization. For the mixture (n-C9+n-C12+n-C15), which has a similar range of T_b as Jet A kerosene (cf. Table 2), this likely leads to a major change of vapor composition over the droplet lifetime.

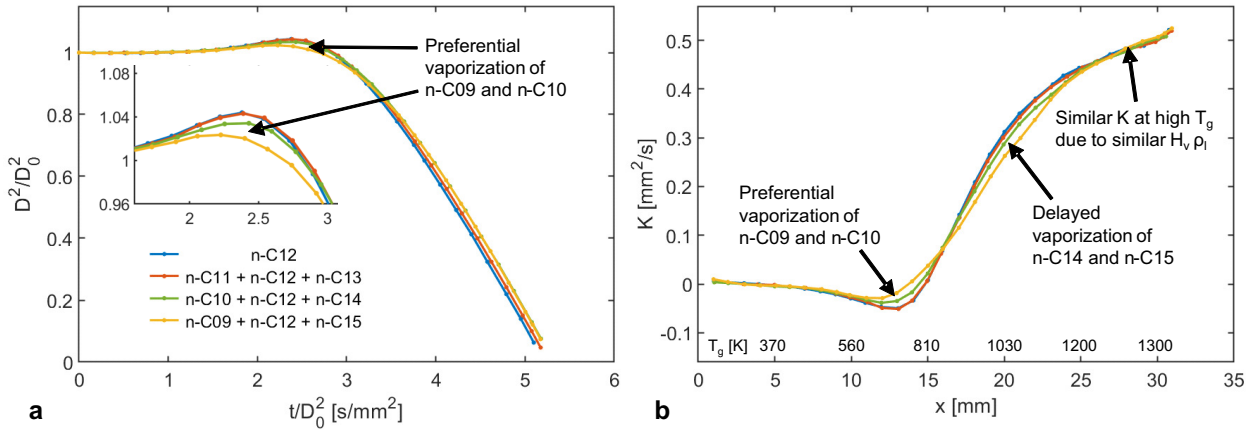

Figure 10: a) Temporal evolution of normalized squared droplet diameter and b) axial evolution of droplet vaporization rate for pure n-dodecane and three mixtures (1:1:1 by vol.) of n-dodecane with two other n-alkanes.

6. Results for transportation fuels

6.1. Fuel properties

This section presents measurements of droplet vaporization for several conventional and alternative fuels for jet and IC engines. These fuels exhibit a large spectrum of different chemical compositions, including components from several different chemical classes. The individual species of the various classes, in turn, exhibit a wide range of physical properties as discussed in Sect. 4.1 and specified in Table 1. For the transportation fuels measured in this work, the chemical composition, density and boiling range are specified in Table 2, and distillation curves are shown in Fig. 11.

The three conventional jet fuels (CJFs) Jet A (POSF 10325), JP-5 (POSF 10289) and JP-8 (POSF 10264) were chosen by the US National Jet Fuels Combustion Program (NJFCP) as a set of fuels that covers the range of properties seen in current petroleum-derived jet fuels [95]. This makes them valuable as a reference for testing the performance of alternative jet fuels (AJFs). Their mass fractions for the different classes of hydrocarbons vary significantly: n-alkanes range between 13.9% for JP-5 and 26.8% for JP-8, iso-alkanes between 18.1% for JP-5 and 39.7% for JP-8, cycloalkanes between 21.6% for JP-8 and 56.3% for JP-5, and aromatics between 11.7% for JP-5 and 15.2% for Jet A. As seen in Fig. 11a, all three CJFs are relatively wide-boiling fuels with notable shifts of T_{50} from 190 °C for JP-8 to 220 °C for JP-5.

The three selected AJFs, namely HEFA, Alcohol-to-jet (AtJ) and Farnesane, are all approved and annexed in ASTM D7566 [7] and have already been operated in commercial passenger flights. HEFA and AtJ can be blended at up to 50% (by vol.) with CJFs, and Farnesane at up to 10% [7]. HEFA is mostly composed of iso-alkanes and has a similar T_{50} as Jet A, but a notably lower T_0 and thus contains more volatile light-end components. AtJ consists almost completely of iso-alkanes and exhibits a rather unusual distillation curve including a very narrow distillate around 180 °C up to 80 Vol% together with a small high-boiling fraction ranging up to 259 °C. Farnesane is a pure C_{15} iso-alkane with a boiling point of 247 °C. All three AJFs are virtually free of aromatics. Further information on the conversion process, feedstock, and composition of these AJFs are provided by Rumizen [7]. The detailed chemical compositions of the CJFs and AJFs have been obtained from GC×GC measurements and are specified in the supplementary material of Ref. [86].

Heating oil extra-light (HEL) is a German petroleum-derived fuel whose physical and chemical properties are generally considered to be similar to those of diesel fuels. Diesel fuels roughly consist of 1/3 (by vol.) cycloalkanes, 1/3 aromatics, 1/6 n-alkanes and 1/6 iso-alkanes [107]. For the composition of the present HEL, only the aromatic content of 29.4% by vol. is known. The distillation curve of HEL (Fig. 11b) covers a wide range between 180 °C and 380 °C, which is significantly higher than that of the jet fuels, and is similar to those of the diesel reference fuels in Ref. [107]. For the measurements discussed in Sect. 6.3, HEL is used as a replacement for diesel fuel.

PRF90 is a 9:1 (by vol.) blend of iso-octane (i.e., 2,2,4-Trimethylpentane) and n-heptane with a narrow boiling range of 98 - 99 °C. Binary blends of primary

Fuel	Composition [% m/m]				ρ [kg/l]	Boiling range [°C]		
	n-alk.	iso-alk.	cycloalk.	arom.	at 20 °C	T_0	T_{50}	T_{100}
Jet A, POSF 10325[a]	20.0	29.4	35.3	15.2	0.803	159	205	271
JP-5, POSF 10289[a]	13.9	18.1	56.3	11.7	0.827	178	220	260
JP-8, POSF 10264[a]	26.8	39.7	21.6	12.0	0.780	150	190	257
AtJ[a]	0.0	99.9	0.1	0.0	0.760	170	181	259
HEFA[a]	15.3	82.3	2.2	0.2	n/a	144	202	256
Farnesane	0.0	100.0	0.0	0.0	0.768[b]		247	
Heating oil EL (≈Diesel)	n/a	n/a	n/a	29.4	n/a	180	275	380
PRF90	10	90	0	0	0.689	98	-	99

[a] Detailed chemical compositions based on GC×GC measurements are available in Ref. [86].
[b] Value for 25 °C from Ref. [106].

Table 2: Chemical composition, density and boiling temperatures for the investigated transportation fuels.

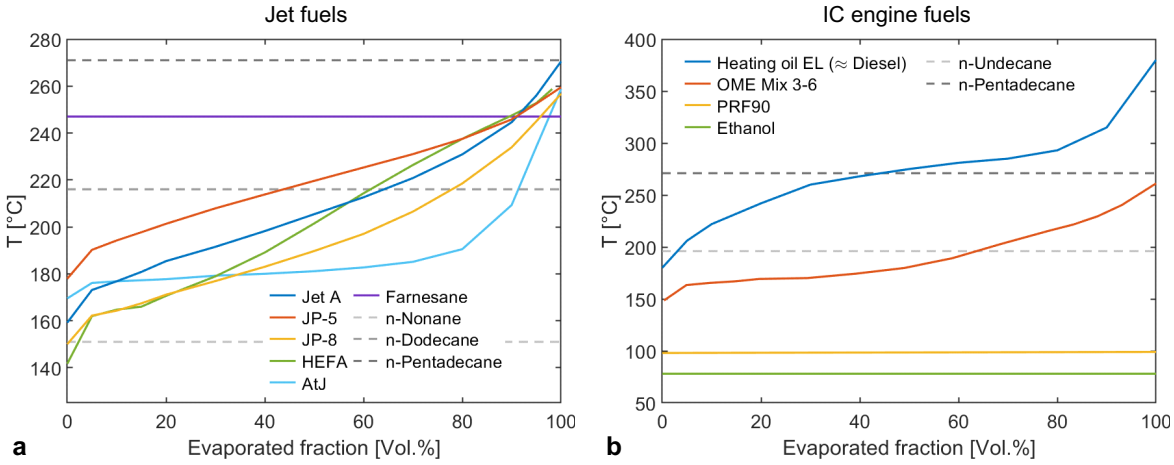

Figure 11: Distillation curves for a) various jet fuels and b) fuels for IC engines.

reference fuels (PRFs) have been widely employed as gasoline surrogates for studies of chemical kinetics and for CFD modeling [108]. In Sect. 6.4, PRF90 is used as a gasoline surrogate for measurements of droplet vaporization, both in pure form and as a blend with ethanol.

6.2. *Jet fuels*

Figure 12 shows the droplet vaporization for the three CJFs together with the results for three n-alkanes. During the early phase of vaporization ($t/D_0^2 \lesssim 3$ s/mm^2, $x \lesssim 16$ mm), where $T_g < 860$ K and K is mostly influenced by T_b as discussed in Sect. 4, the vaporization rates are highest for JP-8 followed by Jet A and then JP-5. This is in good agreement with the respective shifts of boiling temperatures of the CJFs (cf. Fig. 11a). In the later stage ($t/D_0^2 \gtrsim 4$ s/mm^2, $x \gtrsim 20$ mm), where $T_g > 1030$ K and K is largely influenced by $H_v\rho_l$, vaporization rates are still highest for JP-8. This might be explained by the composition of JP-8, which has the highest content of iso-alkanes with low $H_v\rho_l$, and a relatively low content of aromatics with high $H_v\rho_l$ (cf. Tables 1 and 2). The increase in K for JP-8 compared to Jet A and JP-5, however, is rather small and within the range of measurement uncertainties (cf. Sect 2.4).

For comparison, results are also shown for the three n-alkanes n-nonane, n-dodecane and n-pentadecane, whose values of T_b lie near the lower end, middle, and upper end of the boiling range of the CJFs. It can be seen that during the early phase of vaporization ($x \lesssim 16$ mm), the vaporization rate of all three CJFs lies between that of n-nonane and n-dodecane. This shows that during this phase, mainly light-end components vaporize. In the later phase ($x \gtrsim 20$ mm), the CJF vaporization rates are all below that of n-dodecane, indicating that now components heavier than n-dodecane vaporize. The results thus demonstrate that for the present test conditions, a major degree of preferential vaporization occurs for typical jet fuels.

In Fig. 13a, the droplet vaporization is shown for the three AJFs HEFA, AtJ and Farnesane, and compared to the results for the three CJFs. The latter represent the range of properties encountered in currently

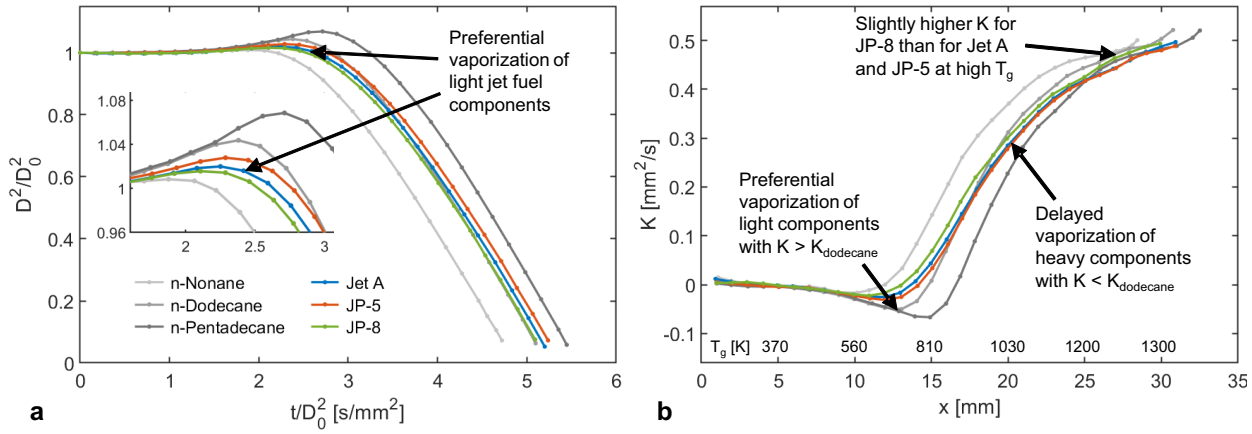

Figure 12: a) Temporal evolution of normalized squared droplet diameter and b) axial evolution of droplet vaporization rate for three CJFs and three n-alkanes.

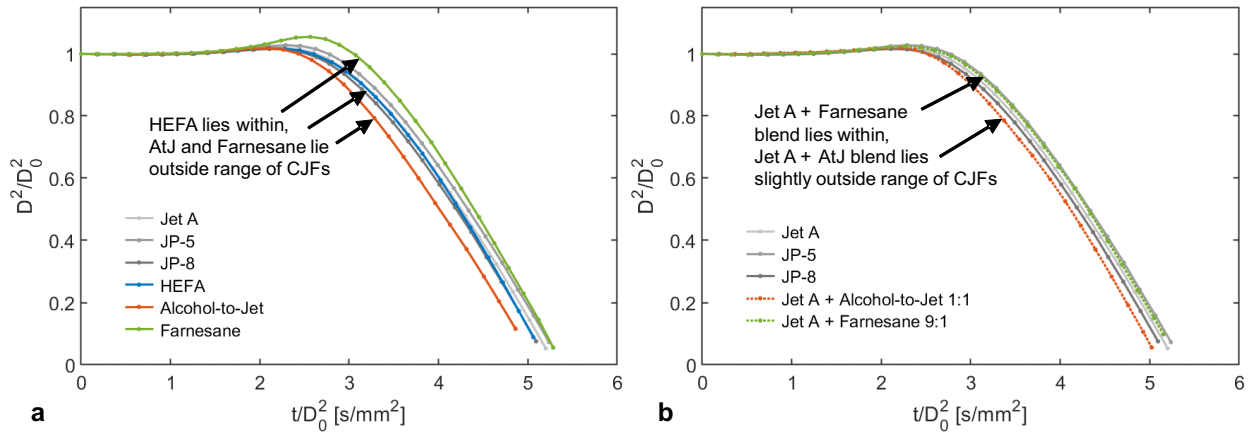

Figure 13: Temporal evolution of normalized squared droplet diameter for a) three AJFs compared to three CJFs, and b) three blends of AJFs and Jet A compared to three CJFs.

used petroleum-derived jet fuels [95] and thus define the target range for the AJFs. The vaporization of HEFA droplets lies within the range of the CJFs, which is expectable since the HEFA distillation curve also largely lies within those of the CJFs. AtJ vaporizes significantly earlier than the CJFs, first due to its comparatively low boiling temperatures, and possibly also because it is almost completely composed of iso-alkanes, which generally have low values of $H_v\rho_l$ (cf. Sect. 4.1, however no measured values are available for AtJ). Farnesane, on the other hand, has a significantly higher boiling temperature than most components of the other CJFs and AJFs, and accordingly its vaporization is for a long time significantly delayed compared to the other fuels. At the end, however, its vaporization rate increases and its lifetime then lies within the range of the CJFs. Again, this might be caused by a low $H_v\rho_l$ of the iso-alkane Farnesane (for which no value for H_v is available).

AtJ and Farnesane, however, can only be used as a blend with a CJF and at a maximum blending ratio of 50% and 10%, respectively [7]. Figure 13b shows measurements for blends of AtJ and Farnesane with Jet A at these maximum ratios. It is seen that the vaporization of the AtJ blend now lies significantly closer to the range of CJFs, but its lifetime is still slightly shorter. The vaporization of the Farnesane blend, on the other hand, now lies completely with the range of CJFs.

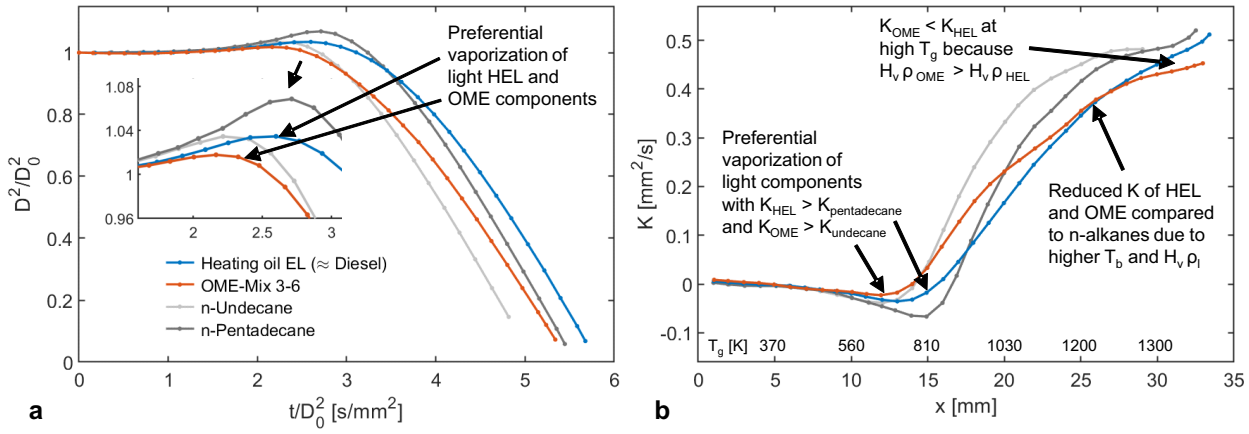

Figure 14: a) Temporal evolution of normalized squared droplet diameter and b) axial evolution of droplet vaporization rate for heating oil EL, a mixture of OME 3-6, and two n-alkanes.

6.3. *Fuels for CI engines*

In the following, the droplet vaporization of a conventional and an alternative diesel-type fuel are compared. As discussed in Sect. 6.1, HEL has a similar composition as diesel fuels, and is thus considered here as a substitute for diesel. OMEs are oxygenated fuel components that can be produced from renewable sources and whose application is mainly concentrated on the field of diesel fuels [99]. While typical species such as $OME_{3–5}$ exhibit physico-chemical and combustion characteristics similar to conventional diesel fuels [99, 109], their boiling temperatures are relatively low compared to the typical range for diesel. The comparison of distillation curves for HEL and a blend of $OME_{3–6}$ in Fig. 11b shows that values of T_b are about 30-100 °C lower for the OME blend. The values of $H_v\rho_l$ for OME_n, on the other hand, are considerably higher than those of n-, iso- and cycloalkanes, and in a similar range as those of aromatics (cf. Table 1), and it is thus expected that the total $H_v\rho_l$ of an OME blend is notably higher than that of HEL / diesel.

Figure 14 shows the droplet vaporization for HEL and a blend of $OME_{3–6}$ together with results for n-undecane and n-pentadecane, whose T_b lie approximately in the middle of the ranges for $OME_{3–6}$ and HEL, respectively (cf. Fig. 11b). During the early phase of vaporization ($t/D_0^2 \lesssim 3$ s/mm^2, $x \lesssim 16$ mm), the vaporization rates for HEL and $OME_{3–6}$ are considerably higher than for n-pentadecane and n-undecane, respectively. This demonstrates that a major degree of preferential vaporization of light components takes place, as seen previously for jet fuels (Sect. 6.2) and bi-/tri-component fuels (Sect. 5). In the later phase ($t/D_0^2 \gtrsim 4$ s/mm^2, $x \gtrsim 20$ mm), vaporization rates of HEL and $OME_{3–6}$ are notably reduced compared to n-pentadecane and n-undecane, respectively. This results from the lower K of the remaining heavy components, and from the higher $H_v\rho_l$ of aromatic species in HEL and of OME species. It is further seen that K is generally higher for $OME_{3–6}$ than for HEL due to the lower T_b of $OME_{3–6}$ until $x \approx 26$ mm. For $x > 26$ mm, however, this ratio reverses and then $K_{HEL} > K_{OME}$. This is likely caused by the overall higher $H_v\rho_l$ of $OME_{3–6}$ compared to HEL mentioned above, and the dominant role of $H_v\rho_l$ at high T_g as discussed in Sect. 4.5. In summary, the measurements of HEL and OME droplet vaporization demonstrate the complex effects of chemical composition, physical properties and gas temperature on the vaporization of practical fuels under technical conditions.

6.4. *Fuels for SI engines*

In this subsection, the vaporization of gasoline engine fuels is studied using PRF90 as a gasoline surrogate, as well as pure ethanol and a 7:3 (by vol.) blend of PRF90 and ethanol. Several experimental studies have shown that the addition of ethanol can lead to reduced emissions such as NO_x, CO and hydrocarbons of gasoline engines, but also to increased soot emissions [24–27, 110]. In either case, these effects have been attributed at least partially to changes of vaporization due to the higher H_v of ethanol. Mixtures of ethanol and hydrocarbons such as iso-octane, however, can exhibit a non-ideal VLE and formation of azeotropic mixtures [110, 111], which can influence droplet vaporization. Bader et al. [98] performed numerical simulations of droplet vaporization for ethanol / iso-octane mixtures

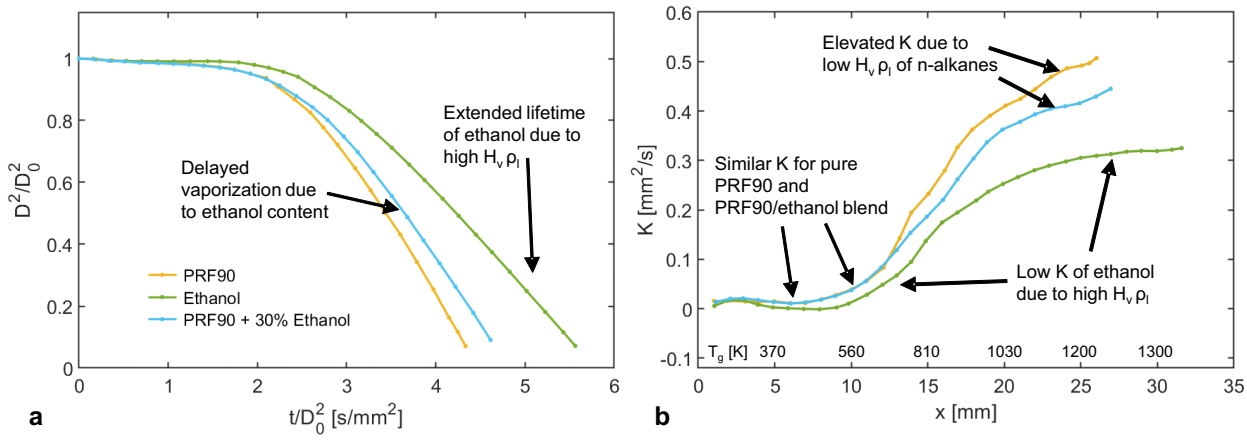

Figure 15: a) Temporal evolution of normalized squared droplet diameter and b) axial evolution of droplet vaporization rate for PRF90, ethanol, and a 7:3 (by vol.) mixture of both.

using both ideal and non-ideal VLE models for numerous conditions including variations of ethanol content, p and T_g, and fixed $D_0 = 100$ μm. Generally, it was found that effects of non-ideal VLE on droplet lifetime can be significant and are strongest for high p and low T_g. However, no experimental validation data was available for the cases studied in this work.

The measured droplet vaporization for PRF90, ethanol and the PRF90/ethanol blend is plotted in Fig. 15. As expected, the vaporization of ethanol droplets is significantly delayed compared to PRF90 droplets, obviously caused by the much higher $H_v\rho_l$ of ethanol. Even during the early phase ($x < 15$ mm) with low T_g, where the lower T_b of ethanol has an enhancing effect on K, $K(x)$ of ethanol is still lower due to its much higher $H_v\rho_l$. The lifetime of the PRF90/ethanol blend droplets between that of PRF90 and ethanol roughly corresponds to the 7:3 blending ratio, and for $x > 15$ mm, the values of $K(x)$ of the blend also lie between PRF90 and ethanol in a similar ratio. The latter suggests that no major preferential vaporization, and thus change of composition has taken place. Interestingly, for $x < 12$ mm, $K(x)$ is almost equal for PRF90 and the PRF90/ethanol blend. This might be caused by a non-ideal VLE leading to a (near-)azeotropic mixture of the blend, which would exhibit both a reduced T_b [111], and an increased H_v [110] compared to pure PRF90 (i.e., mainly iso-octane), such that both effects cancel out and thus $K_{blend} \approx K_{PRF90}$. For higher T_g at $x > 12$ mm, where the influence of $H_v\rho_l$ is stronger, K is then higher for PRF90 due to its lower H_v. A more detailed analysis of the possible role of a non-ideal VLE in this case, however, is beyond the scope of the present work.

Gasoline engines can in principle also be operated with pure ethanol. Ethanol is the most produced biofuel (figures for 2021 from Ref. [8]) and is generally available in two types, namely anhydrous ethanol with a maximum water mass content of 0.7% and hydrous ethanol, i.e., ethanol with a typical water mass content of 6.8% [101]. The water content determines the energy needed for production and has significant effects on engine performance [101, 112]. As for the binary system iso-octane/ethanol discussed above, the system ethanol/water exhibits a non-ideal VLE and an azeotropic mixture for a water mole fraction of about 10% [103, 105]. For water mole fractions of up to 45% (i.e., $\approx$ 20% by vol.), the boiling range of the system remains in the range $78 < T_b < 82$ °C, and thus close to $T_b = 78.3$ °C of pure ethanol (see, e.g., the T-xy diagram in Ref. [113]). The enthalpy of vaporization of the system increases continuously from $H_v \approx 926$ kJ/kg for pure ethanol to $H_v \approx 969$ kJ/kg at 45% water mole fraction [114].

Two recent studies have investigated the vaporization of ethanol–water droplets using numerical simulations. Lupo et al. studied droplets in stagnant air taking into account heat and mass transport in both the liquid and gas phases [65]. Numerous cases with gas temperatures up to 773 K were studied but, on the other hand, no validation measurements were available. Narasu et al. studied bi-component droplets in convective air at T_g of up to 1200 K [102]. In this case the validation data, however, was limited to T_g of up to 473 K and rather large initial diameters of 600 μm.

Figure 16 shows the droplet vaporization for pure ethanol and three mixtures of ethanol with 3.2% (i.e.,

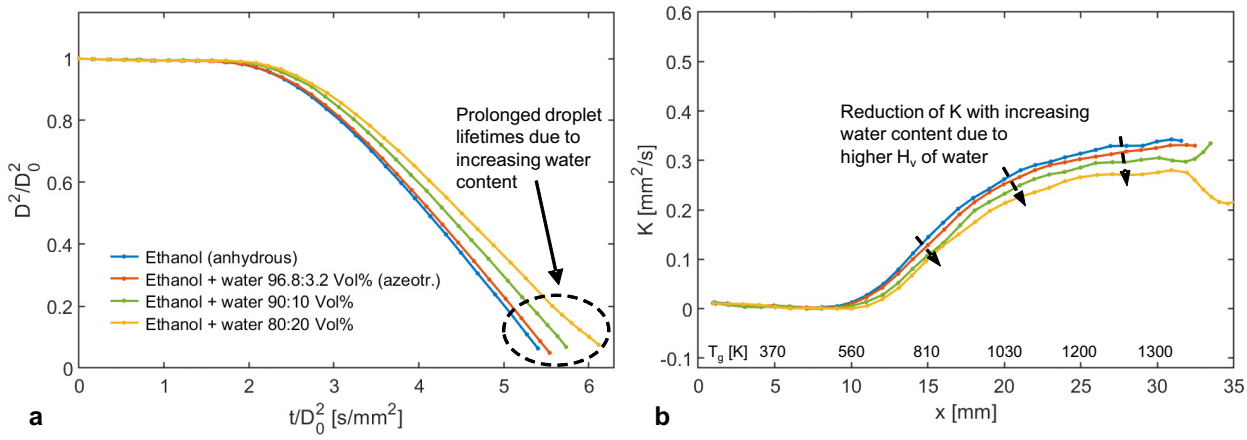

Figure 16: a) Temporal evolution of normalized squared droplet diameter and b) axial evolution of droplet vaporization rate for ethanol with 0%, 3.2%, 10% and 20% (by vol.) water.

the azeotropic mixture), 10% and 20% (by vol.) water. It can be seen that the droplet lifetimes increase, and the vaporization rates decrease continuously with increasing water content. This is obviously caused by the increase of H_v for higher water contents [114] mentioned above. Figure 16b further shows that the relative reduction of K for higher water contents remains similar throughout the droplet lifetime, indicating that no major change of composition, and thus no considerable preferential vaporization of any component takes place. This is expectable since the boiling temperatures of the two components are both limited to a narrow range of $78 < T_b < 82$ °C for up to 20% (by vol.) water as specified above. It is noted that for the strong changes of K at the end of the lifetimes for the cases with 10% and 20% water content, no explanation in terms of either physical mechanism or measurement artifact is currently available. The present measurements provide, to our knowledge, the first experimental data for vaporization of ethanol–water droplets with near-azeotropic compositions under engine-typical temperature conditions, and show that relatively small water contents can lead to notably prolonged droplet lifetimes.

7. Summary and conclusions

In the present work, droplet vaporization has been studied experimentally for numerous, well-specified conventional and alternative fuels for gas turbine and IC engines. A total of 13 single fuel components, five bi- and tri-component mixtures, six conventional and alternative jet fuels and mixtures thereof, and three IC engine fuels and mixtures thereof have been tested. Most of these fuels have been measured for the first time with realistic droplet diameters of $D \approx 77$ μm and technically relevant gas temperatures of up to 1300 K. The experiments employed a recently developed laminar flow channel with free-falling droplets, and the evolution of droplet diameters over travel distance and time was measured using microscopic shadow imaging. The setup thus enabled accurate measurements under well-reproducible ambient conditions for a large set of fuels representing a wide range of chemical classes such as n-alkanes, iso-alkanes, cycloalkanes, aromatics, alcohols and oxymethylene ethers. The main outcomes are as follows:

- The measurements for the single-component fuels, which represent a wide range of values for physical properties such as boiling point T_b, liquid density ρ_l and enthalpy of vaporization, enabled a unique experimental assessment of the temperature-dependent effects of these properties on droplet vaporization. For the enthalpy of vaporization, the enthalpy per mass H_v and the enthalpy per volume $H_v\rho_l$ were considered. For gas temperatures T_g below $\approx$ 1000 K it was found that, as expected, vaporization rates K are mainly governed by T_b, and to a lower degree also by H_v. For the highest temperatures around $\approx$ 1250 K, by contrast, K is almost completely correlated with $H_v\rho_l$ (and to a slightly lower, but still high degree also with H_v). While theoretical considerations discussed in Sect. 3.1 already indicated a predominant effect of H_v on K at high temperatures, this strong correlation is a remarkable result that has, to our

knowledge, not been reported before. While this finding is for now only applicable to the present test conditions ($T_g \approx 1250$ K, atmospheric pressure and low droplet velocity), the result may in principle enable more efficient computations of K based on a reduced number of physical parameters, which might be beneficial for simulations of spray flames with a large number of droplets.

- The mechanisms of preferential vaporization in multi-component fuel droplets have been studied at first using measurements for bi- and tri-component fuel mixtures. By comparing the vaporization rates with those for single-component fuels, a pronounced change of fuel composition over droplet lifetime has been observed, indicating a major degree of preferential vaporization of light components. The effect was strongest for the mixture of n-nonane and n-pentadecane, where after about half of the droplet lifetime, only n-pentadecane was left in the droplet. The results for the tri-component mixtures showed that the extent of preferential vaporization increases when the range of boiling points is wider.

- For both the CJFs and the AJFs, the same temperature-dependent effects of physical properties were observed as for the single-component fuels: For $T_g \lesssim 1000$ K, vaporization is mainly governed by T_b, whereas for higher T_g, slight influences resulting from the different values of $H_v\rho_l$ for different chemical classes such as iso-alkanes and aromatics were seen. Furthermore, for all multi-component jet fuels, a significant degree of preferential vaporization was observed. The vaporization of the alternative HEFA fuel lies within the range of CJFs, whereas AtJ and Farnesane exhibit significant differences in the temporal evolution of vaporization. These differences reduce, as expected, when AtJ and Farnesane are blended with a CJF.

- The comparison of the vaporization of a German heating oil (HEL, with a similar composition as Diesel fuel) with that of a mix of oxymethylene ethers revealed a pronounced preferential vaporization for both fuels, and complex temperature-dependent effects of physical properties and chemical composition: for relatively low T_g, the OME mix vaporizes significantly faster than the HEL due to the lower T_b, whereas later for the higher T_g, vaporization rates are higher for HEL due to its lower $H_v\rho_l$.

- Measurements were also performed for two fuel mixtures that are used in SI engines, namely PRF90 (as a surrogate for gasoline) with ethanol, and ethanol with water. Both mixtures exhibit a non-ideal VLE and to our knowledge, these were the first measurements for these mixtures with realistic droplet size and gas temperatures. In both cases, the vaporization of the mixture is characterized by the much higher H_v of the second component, i.e, ethanol and water, respectively. Significant decreases of vaporization rates and increases of droplet lifetime were observed for mixtures with higher content of the second component. Effects due to the non-ideal VLE, if any, were only seen for $T_g \lesssim 1000$ K, and have not been assessed in detail.

In summary, the present experiments enabled a unique characterization of droplet vaporization for numerous fuels covering a wide range of physical properties and chemical compositions. While the measurements were performed for realistic droplet sizes and gas temperatures, other parameters such as droplet velocity and ambient pressure, however, were markedly lower than in practical combustors. Since these parameters can have major effects on droplet vaporization, future works at more realistic conditions would be desirable. Detailed studies of droplet vaporization at elevated pressure in high-velocity flows are, however, still a major challenge both experimentally and numerically.

8. Acknowledgements

Funding from the EU within the project JETSCREEN (agreement No. 723525) is gratefully acknowledged. We thank T. Edwards and M. Colket from the US NJFCP for providing the fuels Jet A, JP-5 and JP-8, and colleagues of DLR VT-CKA for help with fuel preparation.

References

[1] IEA, World Energy Outlook 2022, IEA, Paris, France, 2022. URL: https://www.iea.org/reports/world-energy-outlook-2022.

[2] European Commission, State of the art on alternative fuels transport systems in the European Union : 2020 update, Publications Office, 2020. URL: https://data.europa.eu/doi/10.2832/937310.

[3] ReFuelEU aviation initiative: Sustainable aviation fuels and the fit for 55 package, 2022. URL: https://www.europarl.europa.eu/thinktank/en/document/EPRS_BRI(2022)698900.

[4] US aviation climate action plan, 2021. URL: https://www.faa.gov/sustainability/aviation-climate-action-plan.

[5] S. Kramer, G. Andac, J. Heyne, J. Ellsworth, P. Herzig, K. C. Lewis, Perspectives on fully synthesized sustainable aviation fuels: direction and opportunities, Front Energy Res 9 (2022) 1040.

[6] J. O'Connor, B. Noble, T. Lieuwen, Renewable Fuels: Sources, Conversion, and Utilization, Cambridge University Press, 2022.

[7] M. A. Rumizen, Qualification of alternative jet fuels, Front Energy Res 9 (2021) 760713.

[8] IEA, Renewables 2022, IEA, Paris, France, 2022. URL: https://www.iea.org/reports/renewables-2022.

[9] J. Liu, L. Wang, P. Wang, P. Sun, H. Liu, Z. Meng, L. Zhang, H. Ma, An overview of polyoxymethylene dimethyl ethers as alternative fuel for compression ignition engines, Fuel 318 (2022) 123582.

[10] C. Voigt, J. Kleine, D. Sauer, R. H. Moore, T. Bräuer, P. Le Clercq, S. Kaufmann, M. Scheibe, T. Jurkat-Witschas, M. Aigner, et al., Cleaner burning aviation fuels can reduce contrail cloudiness, Commun Earth Environ 2 (2021) 114.

[11] T. Schripp, B. E. Anderson, U. Bauder, B. Rauch, J. C. Corbin, G. J. Smallwood, P. Lobo, E. C. Crosbie, M. A. Shook, R. C. Miake-Lye, et al., Aircraft engine particulate matter emissions from sustainable aviation fuels: Results from ground-based measurements during the NASA/DLR campaign ECLIF2/ND-MAX, Fuel 325 (2022) 124764.

[12] R. Teoh, U. Schumann, C. Voigt, T. Schripp, M. Shapiro, Z. Engberg, J. Molloy, G. Koudis, M. E. Stettler, Targeted use of sustainable aviation fuel to maximize climate benefits, Environ Sci Technol 56 (2022) 17246–17255.

[13] J. Heyne, B. Rauch, P. Le Clercq, M. Colket, Sustainable aviation fuel prescreening tools and procedures, Fuel 290 (2021) 120004.

[14] C. A. Moses, P. N. Roets, Properties, characteristics, and combustion performance of Sasol fully synthetic jet fuel, J Eng Gas Turbines Power 131 (2009) 041502.

[15] T. W. Chan, W. A. Chishty, P. Canteenwalla, D. Buote, C. R. Davison, Characterization of emissions from the use of alternative aviation fuels, J Eng Gas Turbines Power 138 (2016).

[16] J. Grohmann, W. O'Loughlin, W. Meier, M. Aigner, Comparison of the combustion characteristics of liquid single-component fuels in a gas turbine model combustor, in: Proc. ASME Turbo Expo, 2016, pp. GT2016–56177.

[17] J. Grohmann, B. Rauch, T. Kathrotia, W. Meier, M. Aigner, Influence of single-component fuels on gas-turbine model combustor lean blowout, J Propuls Power 34 (2018) 97–107.

[18] S. H. Won, N. Rock, S. J. Lim, S. Nates, D. Carpenter, B. Emerson, T. Lieuwen, T. Edwards, F. L. Dryer, Preferential vaporization impacts on lean blow-out of liquid fueled combustors, Combust Flame 205 (2019) 295–304.

[19] N. Rock, I. Chterev, B. Emerson, S. H. Won, J. Seitzman, T. Lieuwen, Liquid fuel property effects on lean blowout in an aircraft relevant combustor, J Eng Gas Turbines Power 141 (2019) 071005.

[20] N. Rock, B. Emerson, J. Seitzman, T. Lieuwen, Near-lean blowoff dynamics in a liquid fueled combustor, Combust Flame 212 (2020) 53–66.

[21] R. Alsulami, S. Lucas, B. Windell, M. Hageman, B. Windom, Experimental assessment of the impact of variation in jet fuel properties on spray flame liftoff height, Appl Energy Combust Sci 7 (2021) 100032.

[22] M. Colket, J. Heyne, Fuel effects on operability of aircraft gas turbine combustors, American Institute of Aeronautics and Astronautics, Inc., 2021.

[23] V. Shastry, E. Riber, L. Gicquel, B. Cuenot, V. Bodoc, Large Eddy Simulations of complex multicomponent swirling spray flames in a realistic gas turbine combustor, Proc Combust Inst (2022). https://doi.org/10.1016/j.proci.2022.08.059.

[24] T. Wallner, S. A. Miers, Combustion behavior of gasoline and gasoline/ethanol blends in a modern direct-injection 4-cylinder engine, Technical Report, SAE Technical Paper, 2008.

[25] D. Turner, H. Xu, R. F. Cracknell, V. Natarajan, X. Chen, Combustion performance of bio-ethanol at various blend ratios in a gasoline direct injection engine, Fuel 90 (2011) 1999–2006.

[26] M. Storch, M. Koegl, M. Altenhoff, S. Will, L. Zigan, Investigation of soot formation of spark-ignited ethanol-blended gasoline sprays with single-and multi-component base fuels, Appl Energy 181 (2016) 278–287.

[27] E. R. M. de Oliveira, C. H. Rufino, P. T. Lacava, Effects of direct injection and mixture enleament on the combustion of hydrous ethanol and an ethanol-gasoline blend in an optical engine, Fuel 327 (2022) 125137.

[28] D. Kim, J. Martz, A. Violi, Effects of fuel physical properties on direct injection spray and ignition behavior, Fuel 180 (2016) 481–496.

[29] L. Esclapez, P. C. Ma, E. Mayhew, R. Xu, S. Stouffer, T. Lee, H. Wang, M. Ihme, Fuel effects on lean blow-out in a realistic gas turbine combustor, Combust Flame 181 (2017) 82–99.

[30] J. Badra, A. Zubail, J. Sim, Numerical investigation into effects of fuel physical properties on gci engine performance and emissions, Energy Fuels 33 (2019) 10267–10281.

[31] X. Hui, K. Kumar, C.-J. Sung, T. Edwards, D. Gardner, Experimental studies on the combustion characteristics of alternative jet fuels, Fuel 98 (2012) 176–182.

[32] D. Carpenter, S. Nates, F. L. Dryer, S. H. Won, Evaluating ignition propensity of high cycloparaffinic content alternative jet fuel by a chemical functional group approach, Combust Flame 223 (2021) 243–253.

[33] K. Kumar, C.-J. Sung, X. Hui, Laminar flame speeds and extinction limits of conventional and alternative jet fuels, Fuel 90 (2011) 1004–1011.

[34] S. H. Won, P. S. Veloo, S. Dooley, J. Santner, F. M. Haas, Y. Ju, F. L. Dryer, Predicting the global combustion behaviors of petroleum-derived and alternative jet fuels by simple fuel property measurements, Fuel 168 (2016) 34–46.

[35] H. Wang, M. A. Oehlschlaeger, Autoignition studies of conventional and Fischer–Tropsch jet fuels, Fuel 98 (2012) 249–258.

[36] S. Jürgens, P. Oßwald, M. Selinsek, P. Piermartini, J. Schwab, P. Pfeifer, U. Bauder, S. Ruoff, B. Rauch, M. Köhler, Assessment of combustion properties of non-hydroprocessed fischer-tropsch fuels for aviation, Fuel Process Technol 193 (2019) 232–243.

[37] J. Zinsmeister, N. Gaiser, J. Melder, T. Bierkandt, P. Hemberger, T. Kasper, M. Aigner, M. Köhler, P. Oßwald, On the diversity of fossil and alternative gasoline combustion chemistry: A comparative flow reactor study, Combust Flame 243 (2022) 111961.

[38] J. Yu, C. Bae, Dimethyl ether (dme) spray characteristics in a common-rail fuel injection system, Proc Inst Mech Eng D: J Automob Eng 217 (2003) 1135–1144.

[39] C. Ejim, B. Fleck, A. Amirfazli, Analytical study for atomization of biodiesels and their blends in a typical injector: surface tension and viscosity effects, Fuel 86 (2007) 1534–1544.

[40] R. Alsulami, B. Windell, S. Nates, W. Wang, S. H. Won, B. Windom, Investigating the role of atomization on flame stability of liquid fuels in an annular spray burner, Fuel 265 (2020) 116945.

[41] T. Buschhagen, R. Z. Zhang, A. J. Bokhart, R. M. Gejji, S. V. Naik, R. P. Lucht, J. P. Gore, P. E. Sojka, C. D. Slabaugh, S. Meyer, Effect of aviation fuel type and fuel injection conditions on non-reacting spray characteristics of a hybrid airblast fuel injector, in: 54th AIAA Aerospace Sciences Meeting, 2016, pp. AIAA 2016–1154.

[42] K. Kannaiyan, R. Sadr, Macroscopic spray performance of alternative and conventional jet fuels at non-reacting, elevated ambient conditions, Fuel 266 (2020) 117023.

[43] M. Broumand, M. S. Khan, S. Yun, Z. Hong, M. J. Thomson, The role of atomization in the spray combustion of a fast pyrolysis bio-oil, Fuel 276 (2020) 118035.

[44] L. Zigan, I. Schmitz, A. Flügel, M. Wensing, A. Leipertz, Structure of evaporating single-and multicomponent fuel sprays for 2nd generation gasoline direct injection, Fuel 90 (2011) 348–363.

[45] F. Yi, R. L. Axelbaum, Stability of spray combustion for water/alcohols mixtures in oxygen-enriched air, Proc Combust Inst 34 (2013) 1697–1704.

[46] L. M. Itani, G. Bruneaux, A. Di Lella, C. Schulz, Two-tracer LIF imaging of preferential evaporation of multi-component gasoline fuel sprays under engine conditions, Proc Combust Inst 35 (2015) 2915–2922.

[47] G. Eckel, J. Grohmann, L. Cantu, N. Slavinskaya, T. Kathrotia, M. Rachner, P. Le Clercq, W. Meier, M. Aigner, LES of a swirl-stabilized kerosene spray flame with a multi-component vaporization model and detailed chemistry, Combust Flame 207 (2019) 134–152.

[48] A. Stagni, L. Esclapez, P. Govindaraju, A. Cuoci, T. Faravelli, M. Ihme, The role of preferential evaporation on the ignition of multicomponent fuels in a homogeneous spray/air mixture, Proc Combust Inst 36 (2017) 2483–2491.

[49] P. Kranz, S. Kaiser, LIF-based imaging of preferential evaporation of a multi-component gasoline surrogate in a direct-injection engine, Proc Combust Inst 37 (2019) 1365–1372.

[50] T. I. Farouk, S. H. Won, F. L. Dryer, Sub-millimeter sized multi-component jet fuel surrogate droplet combustion: Physicochemical preferential vaporization effects, Proc Combust Inst 38 (2021) 3313–3323.

[51] A. Cuoci, C. T. Avedisian, J. D. Brunson, S. Guo, A. Dalili, Y. Wang, M. Mehl, A. Frassoldati, K. Seshadri, J. E. Dec, D. Lopez-Pintor, Simulating combustion of a seven-component surrogate for a gasoline/ethanol blend including soot formation and comparison with experiments, Fuel 288 (2021) 119451.

[52] V. Shastry, Q. Cazeres, B. Rochette, E. Riber, B. Cuenot, Numerical study of multicomponent spray flame propagation, Proc Combust Inst 38 (2021) 3201–3211.

[53] D. Fredrich, A. Giusti, Numerical investigation of multi-component droplet evaporation and autoignition for aero-engine applications, Combust Flame 241 (2022) 112023.

[54] S. J. Lim, A. K. Alwahaibi, F. L. Dryer, S. H. Won, Impacts of preferential vaporization on flashback behaviors of multi-component liquid fuels, Combust Flame 245 (2022) 112300.

[55] L. Luo, Y. C. Liu, Controlling parameters and regimes for preferential vaporization of jet fuel droplet with liquid transport and convection, Fuel 321 (2022) 123817.

[56] M. Bonanni, M. Ihme, Interaction of preferential evaporation and low-temperature chemistry in multicomponent counterflow spray flames, Proc Combust Inst (2022). https://doi.org/10.1016/j.proci.2022.06.006.

[57] J. Tamim, W. L. Hallett, A continuous thermodynamics model for multicomponent droplet vaporization, Chem Eng Sci 50 (1995) 2933–2942.

[58] P. Le Clercq, J. Bellan, Direct numerical simulation of gaseous mixing layers laden with multicomponent-liquid drops: liquid-specific effects, J Fluid Mech 533 (2005) 1087–1104.

[59] P. Le Clercq, N. Doue, M. Rachner, M. Aigner, Validation of a multicomponent-fuel model for spray computations, in: 47th AIAA Aerospace Sciences Meeting, 2009, pp. AIAA 2009–1188.

[60] A. Y. Cooney, S. L. Singer, Modeling multicomponent fuel droplet vaporization with finite liquid diffusivity using coupled algebraic-DQMoM with delumping, Fuel 212 (2018) 554–565.

[61] M. Burger, R. Schmehl, K. Prommersberger, O. Schäfer, R. Koch, S. Wittig, Droplet evaporation modeling by the distillation curve model: accounting for kerosene fuel and elevated pressures, Int J Heat Mass Transfer 46 (2003) 4403–4412.

[62] Y. Ra, R. D. Reitz, A vaporization model for discrete multi-component fuel sprays, Int J Multiphase Flow 35 (2009) 101–117.

[63] A. P. Pinheiro, O. Rybdylova, I. A. Zubrilin, S. S. Sazhin, F. L. Sacomano Filho, J. M. Vedovotto, Modelling of aviation kerosene droplet heating and evaporation using complete fuel composition and surrogates, Fuel 305 (2021) 121564.

[64] S. Sazhin, A. Elwardany, E. Sazhina, M. Heikal, A quasi-discrete model for heating and evaporation of complex multi-component hydrocarbon fuel droplets, Int J Heat Mass Transfer 54 (2011) 4325–4332.

[65] G. Lupo, C. Duwig, A numerical study of ethanol–water droplet evaporation, J Eng Gas Turbines Power 140 (2018) 021401.

[66] M. Elkotb, S. Aly, H. Elsalmawy, Evaporation characteristics of fuel and multifuel droplets, Combust Flame 85 (1991) 300–308.

[67] T. Runge, M. E. Teske, C. Polymeropoulos, Low-temperature vaporization of JP-4 and JP-8 fuel droplets, Atomization Sprays 8 (1998).

[68] J. Wilms, Evaporation of Multicomponent Droplets, Ph.D. thesis, University of Stuttgart, 2005.

[69] H. Ghassemi, S. W. Baek, Q. S. Khan, Experimental study on binary droplet evaporation at elevated pressures and temperatures, Combust Sci Technol 178 (2006) 1031–1053.

[70] H. Nomura, Y. Ujiie, H. Rath, J. Sato, M. Kono, Experimental study on highpressure droplet evaporation using microgravity conditions, Symp (Int) Combust 26 (1996) 1267–1273.

[71] C. Morin, C. Chauveau, I. Gökalp, Droplet vaporisation characteristics of vegetable oil derived biofuels at high temperatures, Exp Therm Fluid Sci 21 (2000) 41–50.

[72] C. Morin, C. Chauveau, P. Dagaut, I. Goekalp, M. Cathonnet, Vaporization and oxidation of liquid fuel droplets at high temperature and high pressure: application to n-alkanes and vegetable oil methyl esters, Combust Sci Technol 176 (2004) 499–529.

[73] H. Ghassemi, S. W. Baek, Q. S. Khan, Experimental study on evaporation of kerosene droplets at elevated pressures and temperatures, Combust Sci Technol 178 (2006) 1669–1684.

[74] W. Hallett, S. Beauchamp-Kiss, Evaporation of single droplets of ethanol–fuel oil mixtures, Fuel 89 (2010) 2496–2504.

[75] P. Deepu, S. Basu, R. Kumar, Vaporization dynamics of functional droplets in a hot laminar air jet, Int J Heat Mass Transfer 56 (2013) 69–79.

[76] I. Javed, S. W. Baek, K. Waheed, G. Ali, S. O. Cho, Evaporation characteristics of kerosene droplets with dilute concentrations of ligand-protected aluminum nanoparticles at elevated temperatures, Combust Flame 160 (2013) 2955–2963.

[77] N. Hashimoto, H. Nomura, M. Suzuki, T. Matsumoto, H. Nishida, Y. Ozawa, Evaporation characteristics of a palm methyl ester droplet at high ambient temperatures, Fuel 143 (2015) 202–210.

[78] K. Han, B. Yang, C. Zhao, G. Fu, X. Ma, G. Song, Experimental study on evaporation characteristics of ethanol–diesel blend fuel droplet, Exp Therm Fluid Sci 70 (2016) 381–388.
[79] J. Wang, X. Wang, H. Chen, Z. Jin, K. Xiang, Experimental study on puffing and evaporation characteristics of jatropha straight vegetable oil (SVO) droplets, Int J Heat Mass Transfer 119 (2018) 392–399.
[80] F. Wang, R. Liu, M. Li, J. Yao, J. Jin, Kerosene evaporation rate in high temperature air stationary and convective environment, Fuel 211 (2018) 582–590.
[81] D. Yang, Z. Xia, L. Huang, L. Ma, Y. Feng, Y. Xiao, Exprimental study on the evaporation characteristics of the kerosene gel droplet, Exp Therm Fluid Sci 93 (2018) 171–177.
[82] Y. Yu, D. Mei, Y. Gao, J. Qi, C. Zhang, Droplet evaporation characteristics of hydrogenated biodiesel-ethanol-diesel ternary fuel, Combust Sci Technol 0 (2023) 1–16.
[83] A. Muelas, P. Remacha, J. Ballester, Droplet combustion and sooting characteristics of UCO biodiesel, heating oil and their mixtures under realistic conditions, Combust Flame 203 (2019) 190–203.
[84] Á. Muelas, J. Carpio, J. Ballester, A. L. Sánchez, F. A. Williams, Pyrolysis effects during high-temperature vaporization of alkane droplets, Combust Flame 217 (2020) 38–47.
[85] D. Honnery, D. Nguyen, J. Soria, Microdroplet evaporation under increasing temperature conditions: Experiments and modelling, Fuel 105 (2013) 247–257.
[86] M. Stöhr, S. Ruoff, B. Rauch, W. Meier, P. Le Clercq, Droplet vaporization for conventional and alternative jet fuels at realistic temperature conditions: Systematic measurements and numerical modeling, Proc Combust Inst 38 (2021) 3269–3276.
[87] P. Weigand, R. Lückerath, W. Meier, Documentation of flat premixed laminar CH_4/air standard flames: temperatures and species concentrations, Technical Report, Institute of Combustion Technology, German Aerospace Center (DLR), 2003.
[88] M. Heitor, A. Moreira, Thermocouples and sample probes for combustion studies, Prog Energy Combust Sci 19 (1993) 259–278.
[89] C. Law, Recent advances in droplet vaporization and combustion, Prog Energy Combust Sci 8 (1982) 171–201.
[90] S. S. Sazhin, Advanced models of fuel droplet heating and evaporation, Prog Energy Combust Sci 32 (2006) 162–214.
[91] W. Sirignano, Fluid Dynamics and Transport of Droplet and Sprays, Second ed., Cambridge University Press, 2010.
[92] A. H. Lefebvre, V. G. McDonell, Atomization Sprays, Second ed., CRC press, 2017.
[93] C. K. Law, Multicomponent droplet combustion with rapid internal mixing, Combust Flame 26 (1976) 219–233.
[94] A. Makino, C. K. Law, On the controlling parameter in the gasification behavior of multicomponent droplets, Combust Flame 73 (1988) 331–336.
[95] J. T. Edwards, Reference jet fuels for combustion testing, in: 55th AIAA aerospace sciences meeting, 2017, pp. AIAA 2017–0146.
[96] A. K. Agarwal, Biofuels (alcohols and biodiesel) applications as fuels for internal combustion engines, Prog Energy Combust Sci 33 (2007) 233–271.
[97] B. R. Kumar, S. Saravanan, Use of higher alcohol biofuels in diesel engines: A review, Renewable Sustainable Energy Rev 60 (2016) 84–115.
[98] A. Bader, P. Keller, C. Hasse, The influence of non-ideal vapor–liquid equilibrium on the evaporation of ethanol/iso-octane droplets, Int J Heat Mass Transfer 64 (2013) 547–558.
[99] K. Hackbarth, P. Haltenort, U. Arnold, J. Sauer, Recent progress in the production, application and evaluation of oxymethylene ethers, Chem Ing Tech 90 (2018) 1520–1528.
[100] A. Omari, B. Heuser, S. Pischinger, C. Rüdinger, Potential of long-chain oxymethylene ether and oxymethylene ether-diesel blends for ultra-low emission engines, Appl Energy 239 (2019) 1242–1249.
[101] R. C. Costa, J. R. Sodré, Hydrous ethanol vs. gasoline-ethanol blend: Engine performance and emissions, Fuel 89 (2010) 287–293.
[102] P. Narasu, S. Boschmann, P. Pöschko, F. Zhao, E. Gutheil, Modeling and simulation of single ethanol/water droplet evaporation in dry and humid air, Combust Sci Technol 192 (2020) 1233–1252.
[103] W. M. Haynes, D. R. Lide, T. J. Bruno, CRC Handbook of Chemistry and Physics, CRC press, 2016.
[104] R. H. Boyd, Some physical properties of polyoxymethylene dimethyl ethers, J Polym Sci 50 (1961) 133–141.
[105] P. Stephan, S. Kabelac, M. Kind, H. Martin, D. Mewes, K. Schaber, VDI Heat Atlas, Second ed., Springer, 2010.
[106] F. G. Fischer, Die Konstitution des Phytols, Liebigs Ann 464 (1928) 69–90.
[107] C. J. Mueller, W. J. Cannella, T. J. Bruno, B. Bunting, H. D. Dettman, J. A. Franz, M. L. Huber, M. Natarajan, W. J. Pitz, M. A. Ratcliff, et al., Methodology for formulating diesel surrogate fuels with accurate compositional, ignition-quality, and volatility characteristics, Energy Fuels 26 (2012) 3284–3303.
[108] S. M. Sarathy, A. Farooq, G. T. Kalghatgi, Recent progress in gasoline surrogate fuels, Prog Energy Combust Sci 65 (2018) 67–108.
[109] L. Lautenschütz, D. Oestreich, P. Seidenspinner, U. Arnold, E. Dinjus, J. Sauer, Physico-chemical properties and fuel characteristics of oxymethylene dialkyl ethers, Fuel 173 (2016) 129–137.
[110] L. Chen, R. Stone, Measurement of enthalpies of vaporization of isooctane and ethanol blends and their effects on PM emissions from a GDI engine, Energy Fuels 25 (2011) 1254–1259.
[111] C.-C. Wen, C.-H. Tu, Vapor–liquid equilibria for binary and ternary mixtures of ethanol, 2-butanone, and 2, 2, 4-trimethylpentane at 101.3 kPa, Fluid Phase Equilib 258 (2007) 131–139.
[112] R. Munsin, Y. Laoonual, S. Jugjai, Y. Imai, An experimental study on performance and emissions of a small SI engine generator set fuelled by hydrous ethanol with high water contents up to 40%, Fuel 106 (2013) 586–592.
[113] R. Battisti, C. A. Claumann, C. Marangoni, R. A. Machado, Optimization of pressure-swing distillation for anhydrous ethanol purification by the simulated annealing algorithm, Braz J Chem Eng 36 (2019) 453–469.
[114] D. Newsham, E. Mendez-Lecanda, Isobaric enthalpies of vaporization of water, methanol, ethanol, propan-2-ol, and their mixtures, J Chem Thermodyn 14 (1982) 291–301.